

677/85

JPL Publication 01-16



# **A Numerical Simulation of Supersonic Turbulent Convection Relating to the Formation of the Solar System**

*A. J. R. Prentice  
Monash University  
Victoria 3800  
Australia*

*C. P. Dyt  
CSIRO Division of Petroleum Resources  
Kensington, Western Australia 6151  
Australia*

**National Aeronautics and  
Space Administration**

**Jet Propulsion Laboratory  
California Institute of Technology  
Pasadena, California**

---

*December 2001*





# **A Numerical Simulation of Supersonic Turbulent Convection Relating to the Formation of the Solar System**

*A. J. R. Prentice*  
*School of Mathematical Sciences*  
*Monash University*  
*Victoria 3800*  
*Australia*  
*E-mail: [andrew.prentice@sci.monash.edu.au](mailto:andrew.prentice@sci.monash.edu.au)*

*C. P. Dyt*  
*CSIRO Division of Petroleum Resources*  
*Kensington, Western Australia 6151*  
*Australia*  
*E-mail: [chris.dyt@csiro.au](mailto:chris.dyt@csiro.au)*

**National Aeronautics and  
Space Administration**

**Jet Propulsion Laboratory  
California Institute of Technology  
Pasadena, California**

This publication was prepared by the Jet Propulsion Laboratory,  
California Institute of Technology, under a contract with the  
National Aeronautics and Space Administration.

## ABSTRACT

A flux-corrected transport scheme due to Zalesak (1979) is used to numerically simulate thermal convection in a two-dimensional layer of ideal, diatomic gas, which is heated from below and stratified gravitationally across many pressure scale heights. The purpose of this calculation is to mimic the physical conditions in the outer layers of the protosolar cloud [PSC] from which the Solar System formed. The temperature  $T_0$  at the top boundary ( $z = 0$ ) and the dimensionless temperature gradient  $\theta = (d/T_0)\partial T/\partial z$  at the base of the layer of thickness  $d$  are kept fixed, with  $\theta = 10$ . The initial atmosphere is uniformly superadiabatic, having polytropic index  $m_{\text{in}} = 1$ . Because the Reynolds number of the real atmosphere is so large, a subgrid-scale [SGS] turbulence approximation due to Smagorinsky (1963) is used to model the influence of motions whose length scale is less than the computational grid size.

The flow soon evolves to a network of giant convective cells, which span the whole layer. At cell boundaries the downflows are spatially concentrated and rapid while the upflows are broad and sluggish. The peak downflow Mach number is  $M_{\text{peak}} = 1.1$  at depth  $z = 0.55d$ . The descent of the cold gas eliminates much of the initial superadiabatic structure of the atmosphere for  $z \gtrsim 0.1d$ , thereby reducing the long-term mean temperature gradient  $d\bar{T}_{\text{lt}}/dz$  and causing a sharp rise in mean density  $\bar{\rho}_{\text{lt}}(z)$  towards the base.

In the top 10 percent of depth, SGS modelling causes  $d\bar{T}_{\text{lt}}/dz$  to increase sharply. A steep density inversion occurs with  $\bar{\rho}_{\text{lt}}(0)$  rising to 3.5 times the initial density  $\rho_0$  at the top boundary. This result gives new credibility to the modern Laplacian theory [MLT] of Solar System origin. Here a postulated 35-fold density increase at the surface of the PSC causes the shedding of discrete gas rings at the observed mean orbital spacings of the planets (Prentice 1978a, 2001a). Even so, further numerical simulations, corresponding to higher values of  $\theta$ , that may yield values  $M_{\text{peak}} \simeq 3$  and  $\bar{\rho}_{\text{lt}}(0)/\rho_0 \simeq 35$ , are required before the MLT can be considered to be valid.



# TABLE OF CONTENTS

ABSTRACT .....	iii
1. INTRODUCTION.....	1
1.1 Background .....	1
1.2 The Modern Laplacian Theory of Solar System origin.....	2
1.3 Layout.....	4
2. PREVIOUS SIMULATIONS OF SUPERSONIC THERMAL CONVECTION .....	6
2.1 The mismatch between the needs of the MLT and results of existing numerical simulations .....	6
2.2 Early subsonic simulations.....	6
2.3 Supersonic turbulent convection in the regime of low Rayleigh and Reynolds numbers .....	8
2.4 A way forward: the need to model the regimes of very high Rayleigh and Reynolds numbers.....	9
3. THE SUBGRID-SCALE TURBULENT VISCOSITY FORMALISM .....	10
3.1 The problem of high Reynolds number.....	10
3.2 The velocity-dependent turbulent viscosity $\nu_t$ .....	11
3.3 The turbulent thermal diffusivity $\kappa_t$ .....	12
4. EQUATIONS AND PARAMETERS OF THE MODEL ATMOSPHERE .....	14
4.1 The gas dynamic equations .....	14
4.2 The boundary conditions.....	16
5. THE NUMERICAL SCHEME .....	18
5.1 The flux-corrected transport scheme.....	18
5.2 Specifying the computational domain.....	18
6. RESULTS: FLOW STRUCTURE AND ENERGY FLUXES .....	19
6.1 Early stages of the convection.....	19
6.2 The long-term, quasi-equilibrium state .....	20
6.3 Energy transfer through the atmosphere .....	22
6.4 Comparison with a previous simulation.....	25

7.	RESULTS: THE LONG-TERM PHYSICAL STRUCTURE AND TURBULENT STATE OF THE ATMOSPHERE.....	26
7.1	The long-term mean profiles of temperature, density, and pressure.....	26
7.2	Origin of the steepened temperature gradient and density inversion at the top of the atmosphere .....	28
7.3	The wave number spectrum of kinetic energy .....	30
8.	CONCLUSIONS AND DISCUSSION.....	32
8.1	Summary of main results.....	32
8.2	Implications for the Modern Laplacian Theory .....	35
8.3	Finale.....	37
	ACKNOWLEDGMENTS.....	39
	REFERENCES.....	39

## LIST OF FIGURES

Figure 1.	Total energy fluxes at the base and top of the atmosphere versus elapsed time.....	45
Figure 2.	Contours of temperature and density and the velocity streamlines at time $t = 60$ .....	46
Figure 3.	The four components of mean vertical energy flux versus atmospheric depth $z$ at time $t = 60$ .....	47
Figure 4.	Phase diagrams of kinetic energy and enthalpy flux at time $t = 60$ .....	48
Figure 5.	The four components of mean vertical energy flux versus horizontal distance $x$ at time $t = 60$ .....	49
Figure 6.	Mean temperature $\bar{T}(z, t)$ versus atmospheric depth $z$ .....	50
Figure 7.	Mean density $\bar{\rho}(z, t)$ versus atmospheric depth $z$ .....	51
Figure 8.	Mean pressure $\bar{p}(z, t)$ versus atmospheric depth $z$ .....	52
Figure 9.	Wave number spectrum of specific kinetic energy $\langle E(k_1, k_2) \rangle$ .....	53



# 1. INTRODUCTION

## 1.1 Background

The process by which the Solar System was formed remains poorly understood despite the great wealth of new information about its physical and chemical structure that has been obtained through interplanetary space probes and Earth-based observations. A major problem in reconstructing what happened in the past is that much of the detail of the early Solar System record has been lost. Such a loss has occurred both through internal processes, such as plate tectonics within the Earth which has erased the initial crater record, and through external interactions. An example of the latter is tidal action. The three inner Galilean satellites of Jupiter most likely experienced profound structural change at some unknown point in the past as the result of heat generated by the frictional dissipation of tidal energy produced during passage through orbital resonances (Tittlemore 1990; Malhotra 1991).

In attempting to understand how the Solar System was formed, it is very important, therefore, to first concentrate on explaining the broad physical and chemical features that have remained unchanged since the beginning. Such features include the near circularity of the planetary and regular satellite orbits and the nearly uniform gradation with orbital distance of the uncompressed mean densities of the planets and Galilean satellites. Such theories, which can satisfactorily account for these basic features, can then be further tested by their ability to explain other, secondary, features and to make useful predictions that can be checked by future observations. Even so, as Woolfson (1993) has noted, ‘the nature of the cosmogonic problem ... is that the term *correct* cannot be applied to any theory.’ Further, owing to the

complexity of the Solar System, it is very unlikely that its structure can be accounted for by any one single process, or theory, anyway. It is important, therefore, to keep track of the merits of all physically plausible theories. Woolfson (1978, 2000) himself has been responsible for the development of the Capture Theory of Solar System origin. This theory is a modern, quantitative extension of the wandering star hypothesis of Jeans (1917) and Jeffreys (1918). It is able to explain many important features of the Solar System, including the broad distributions of planetary mass and angular momentum. It can also account for several minor features as well, such as the inclinations of the planetary spin axes, especially that of Uranus, and also the tilt of the solar spin axis relative to the mean plane of the planetary system.

## **1.2 The Modern Laplacian Theory of Solar System origin**

The present paper is concerned with the mathematical foundation of the modern Laplacian theory of Solar System origin (Prentice 1978a, 1978b, 1996a, 1996b, 2001a; Prentice & ter Haar 1979). This theory, dubbed the MLT, is a modern reformulation of the original nebula hypothesis of Laplace (1796) according to which the planets condensed close to their present orbital radii from a concentric system of circular gas rings. These rings were shed somehow from the equator of the primitive cloud of gas, which had contracted inwards from the orbit of Neptune to form the Sun, some  $4.5 \times 10^9$  yr ago.

Laplace did not specify the physical mechanism by which the protosolar cloud (hereafter, the PSC) abandoned discrete gas rings. In the MLT it is suggested that this mechanism is

supersonic turbulent convection driven by the heat released through the steady gravitational contraction of the cloud. It is assumed that near the surface of the PSC there existed a radial turbulent stress  $\langle \rho_t v_t^2 \rangle$  arising from buoyancy-driven thermal convection having magnitude  $\sim 30\text{--}40$  times the local gas pressure  $p_{\text{gas}} = \rho \mathcal{R} T / \mu$ . Here  $\rho_t$  and  $v_t$  are the mass density and radial velocity of moving material; and  $\rho$ ,  $T$ , and  $\mu$  are the local mean density, temperature, and molecular weight.  $\mathcal{R}$  is the gas constant. Turbulent stress of such magnitude implies convective speeds  $v_t$  that are nearly an order of magnitude larger than the local isothermal sound speed  $v_{\text{iso}} = \sqrt{\mathcal{R} T / \mu}$ . If such a stress did exist it would greatly expand the outer tenuous layers of the cloud, so lowering its axial moment-of-inertia factor  $f$  (Prentice 1973). This means that the PSC is able to rid excess spin angular momentum at the expense of losing very little mass from its equator, assuming that the turbulent viscosity arising from the convection causes the cloud interior to rotate with a nearly uniform angular velocity (Prentice 1978a). This helps account for the low mass of the planetary system relative to the Sun.

Next, it is supposed that the degeneration of all radial turbulent motions in the convectively stable layers above the photosurface results in a very steep density inversion by the factor

$$\rho_+ / \rho_- = 1 + [\langle \rho_t v_t^2 \rangle / p_{\text{gas}}]_{\text{ph}} \sim 30\text{--}40 \quad (1)$$

Here  $\rho_-$  denotes the gas density of the fully turbulent material just below the photosurface [ph] and  $\rho_+$  is the density at the base of the lid of non-turbulent gas just above it. When rotation is taken into account, the spherical lid of non-turbulent gas evolves into a dense, belt-like structure at the equator of the fully rotating cloud. The contracting PSC is now able

to dispose of excess spin angular momentum by detaching a discrete family of orbiting gas rings whose orbital radii  $R_n$  ( $n = 0, 1, 2, \dots$ ) satisfy the equations

$$R_n/R_{n+1} \approx [1 + m_n/M_n f_n]^2 \quad (2)$$

Here  $m_n$  denotes the mass of the  $n$ th ring, and  $M_n$  and  $f_n$  are the residual mass and moment-of-inertia factor of the cloud at the moment of ring detachment. Hence, if the gravitational contraction occurs homologously, so that both  $m_n/M_n$  and  $f_n$  stay sensibly constant, then the  $R_n$  form a geometric sequence similar to the Titius-Bode law of planetary distances. Typically if  $\langle \rho_t v_t^2 \rangle \approx 35 p_{\text{gas}}$ , so that  $\rho_+/ \rho_- \approx 35$ , then  $m_n/M_n \approx 0.006$ ,  $f_n \approx 0.02$  and  $R_n/R_{n+1} \approx 1.7$ . The observed mean geometric spacing ratio of the planets is  $\langle R_n/R_{n+1} \rangle_{\text{obs}} \approx 1.72 \pm 0.23$ .

A more detailed account of the workings of the MLT, especially in regard to its capacity to make detailed quantitative predictions for the bulk chemical structure of the planetary system and for the physical, orbital, and bulk chemical structure of the Galilean satellites of Jupiter, is given elsewhere (Prentice 2001a, 2001b, 2001c).

### 1.3 Layout

The rest of this paper is arranged as follows. In Section 2, attention is drawn to the 10-fold discrepancy which exists between the size of the radial turbulent stress  $\langle \rho_t v_t^2 \rangle$  that is needed for the PSC to shed discrete gas rings at its equator and the maximum dynamical pressures  $\rho w^2$  that emerge from actual numerical simulations of supersonic thermal convection (Cattaneo, Hurlburt, & Toomre 1990; Malagoli, Cattaneo, & Brummell 1990; Cattaneo et al.

1991). Here  $w$  denotes the vertical component of the large-scale convective flow. It is then pointed out that all existing computational simulations are restricted to flows having Rayleigh and Reynolds numbers that are typically a factor  $\sim 10^6$  less than the values characteristic of true stellar and protosolar atmospheres. This restriction is imposed by the limit on computational capacity. Essentially, the present simulations are unable to include the contributions of the small-scale turbulent flows whose scale is less than the computational grid size. To get around this problem, a subgrid-scale eddy viscosity formalism devised by Smagorinsky (1963) for use in meteorology is introduced in Section 3.

Next, the mathematical equations and parameters which control compressible thermal convection in a two-dimensional [2D] model atmosphere are set out in Section 4. In Section 5, a flux corrected transport scheme constructed earlier by Dyt & Prentice (1998) for numerically solving the system of gas dynamic equations is briefly outlined. The results of a complete computational simulation for the onset and development of supersonic thermal convection in a model atmosphere which has the same boundary conditions and defining parameters as those used by Cattaneo et al. (1990, 1991), but with the viscosity and thermal diffusivity now due to subgrid-scale turbulence rather than molecular diffusion, are presented in Sections 6 and 7. The highlight of these calculations is the discovery of a sharp and significant density inversion at the top boundary of the atmosphere. The important implications of this exciting discovery for the MLT are discussed in the concluding Section 8. These results were first reported to the 32<sup>nd</sup> annual meeting of the AAS Division of Planetary Sciences in Pasadena, California (Prentice & Dyt 2000).

## 2. PREVIOUS SIMULATIONS OF SUPERSONIC THERMAL CONVECTION

### 2.1 The mismatch between the needs of the MLT and results of existing numerical simulations

Despite the potential of the MLT as a good-working hypothesis of Solar System origin, a major stumbling block is the model's dependence on very large non-thermal stresses arising from supersonic turbulent convection. Stresses  $\langle \rho v_t^2 \rangle$  of magnitude up to  $\sim 35$  times the local gas pressure  $p_{\text{gas}} = \rho \mathcal{R}T/\mu$  are needed to produce a density inversion at the photosurface of the PSC, which is large enough for the cloud to shed discrete gas rings. Such stresses imply mean convective speeds  $v_t$  that are some five times larger than the local adiabatic sound speed  $v_{\text{ad}} = \sqrt{\gamma \mathcal{R}T/\mu}$ , where  $\gamma = 1.4$  is the ratio of specific heats for a diatomic gas. *Here then is the problem:* Detailed numerical simulations of very strong thermal convection in thermally unstable atmospheres that are stratified gravitationally across many pressure scale heights  $h = \mathcal{R}T/\mu g$ , where  $g$  is the local gravitational acceleration, indicate that the local Mach number  $M = \langle v_t \rangle / v_{\text{ad}}$  is always less than  $\sim 3$ . A brief account of these simulations follows.

### 2.2 Early subsonic simulations

In one of the earliest computational simulations of compressible thermal convection in a model stellar atmosphere, Hurlburt, Toomre, & Massaguer (1984) discovered the existence of strong, downward-directed plumes, which traversed the full depth of the layer. But the Mach numbers of these flows were everywhere subsonic. Similar results were also reported by

Chan, Sofia, & Wolff (1982) and Chan & Sofia (1986, 1989). Both of the above groups, however, had assumed only a modest level of convective instability as measured by the dimensionless Rayleigh number  $Ra = L^2 U^2 / \nu \kappa$ . Here  $L$  denotes a characteristic length scale for the system,  $U$  (or  $\langle v_t \rangle$ ) is a characteristic velocity of the flow, and  $\nu$  and  $\kappa$  denote the molecular kinematic viscosity and thermal diffusivity, respectively. No convective motion at all ensues unless  $Ra$  exceeds a critical value  $\sim 660$  (Gough, Moore, Spiegel, & Weiss 1976). And unless  $Ra \gtrsim 5 \times 10^5$ , the convective flow remains steady, subsonic, and non-turbulent. Essentially if  $Ra \lesssim 5 \times 10^5$ , the rate of thermal diffusion by molecular processes is sufficiently rapid to prevent the development of density and temperature fluctuations large enough to make the convection turbulent.

Recently, Porter, & Woodward (2000) have complemented the study of Hurlburt et al. (1984) and that of the Chan & Sofia group by taking advantage of greatly improved computational power to increase spatial resolution. This work has led to a much better understanding of the production of small-scale features in the convective flow. A major distinction between the two sets of calculations is that Porter & Woodward assume that the fluid has no explicit viscosity. This means that they are modelling a slightly different physical system. Even so, it is reassuring that most of the large-scale flow features reported earlier, such as the existence of strong downflow plumes which traverse the full depth of the modelled atmosphere, are retained in the passage to higher resolution. They report a maximum Mach number of 0.8 in a horizontal flow near the top boundary.

### 2.3 Supersonic turbulent convection in the regime of low Rayleigh and Reynolds numbers

Cattaneo et al. (1990) were the first to carry out a numerical simulation that demonstrated the existence of time-dependent, supersonic turbulent convection. They modelled a 2D section of a thermally unstable layer of an ideal gas having a ratio of specific heats  $\gamma = 1.4$ . The dimensionless, uniform temperature gradient of the initially stationary atmosphere of thickness  $d$  and upper boundary temperature  $T_0$  is  $\theta = (d/T_0)\partial T/\partial z = 10$ , where  $z$  denotes the vertical distance below the upper boundary  $z = 0$  and  $0 \leq z \leq d$ . The initial polytropic index is  $m_{\text{in}} = 1$ . Again it is assumed that the thermal conductivity and shear viscosity are constant and arise entirely from molecular diffusion. For  $Ra \approx 5 \times 10^5$ , Cattaneo et al. (1990) report a peak Mach number of 2.7 in a horizontal flow near the top boundary. Malagoli et al. (1990) extended this simulation to three dimensions [3D] and found that many of the features seen in the 2D calculations survive to 3D. At depth  $z = 0.125d$ , the maximum Mach number oscillates about an average of 1.55. This implies a maximum ratio of vertical dynamical stress  $\rho w^2$  to gas pressure that is  $\gamma M^2 \approx 3\text{--}4$ . This falls a long way short of the value  $\sim 35$  needed by the MLT.

The most vigorous case of 3D compressible convection that has so far been investigated is that of Cattaneo et al. (1991). This case, corresponding to  $Ra \approx 1.3 \times 10^6$ , defines the upper limit of their computational capacity. Regions of supersonic flow are now always present near the upper boundary of the modelled zone. The spatial structure of the flow is much more complex than that of the low  $Ra$  simulations. Strong cooling at the upper boundary results in



the production of a layer of low entropy gas and a network of strong, spatially concentrated downflows. These extend to the base of the atmosphere. The upflows, however, tend to be broad, sluggish, and less organized. The same general picture was also observed by Dyt & Prentice (1998) in a modest 2D simulation of supersonic thermal convection. They pointed out that the asymmetry in the relative strengths of the upflows and downflows is directly traceable to the condition of fixed temperature that is imposed at the upper boundary. This condition ensures a constant supply of dense, low entropy gas whose downfall readily cools the deep interior of the atmosphere. Again supersonic speeds are achieved in the downflows, but the maximum dynamical stress barely exceeds the gas pressure.

## **2.4 A way forward: the need to model the regimes of very high Rayleigh and Reynolds numbers**

Now in all of the above numerical simulations it has only been possible to model the thermal convection at the low end of the turbulence regime. This is because the available computational capacity (up to  $96^3$  grid points in the 3D simulations of Cattaneo et al. (1991)), places a corresponding upper limit  $\sim 10^6$  on the maximum Rayleigh number  $Ra$  of any convective flow that can be spatially resolved at every length scale. But for a true stellar atmosphere  $Ra \gtrsim 10^{15}$  (de Loore 1970). A similar estimate  $\sim 10^{12}$  applies to the other important measure of the state of turbulence in the flow, namely the Reynolds number  $Re = LU/\nu$  (Cattaneo et al. 1991). It is clear, therefore, that there must be many important aspects of supersonic turbulent convection that have so far remained unmodelled. The real

problem to deal with then is the great range of distance scales across which fully developed turbulence operates. A scheme for dealing with this situation is introduced below.

### 3. THE SUBGRID-SCALE (SGS) TURBULENT VISCOSITY FORMALISM

#### 3.1 The problem of high Reynolds number

Perhaps the most important piece of information needed to numerically simulate turbulent convection in a stellar/protosolar atmosphere is the specification of viscosity and its relation to the spatial resolution of the flow. Now as mentioned in Section 2, the Reynolds number, viz  $Re = LU/\nu$ , of the solar atmosphere is estimated to be of order  $10^{12}$  (de Loore 1970). Here  $L$  and  $U$  are the characteristic length and speed of the convection, and  $\nu$  is the molecular kinematic viscosity. The smallest identifiable feature in the convective flow has a size comparable with the Kolmogorov length scale  $l_K = (\nu^3/\varepsilon)^{1/4}$ , where  $\varepsilon$  is the bulk viscous dissipation rate per unit mass (Landahl & Mollo-Christensen 1992, p.10). This latter quantity has the same order of magnitude as the kinetic energy injection rate  $\sim U^3/L$  of the largest eddies. To resolve all spatial features of the flow would thus require  $L/l_K = O(Re^{3/4}) = 10^9$  grid points in each coordinate direction. To completely resolve a 3D flow will require around  $10^{27}$  grid points. This, of course, is an impossible task for any computer.

An obvious solution to the problem of high  $Re$  is to drastically increase the effective viscosity  $\nu$ . This, however, raises a new problem in that a different physical system is now being modelled. It is for this reason that the Cattaneo group have adopted a ‘bottom-up’

approach to the problem. That is, they keep  $\nu$  fixed as a constant, corresponding to the molecular viscosity value, and work the calculations up to the maximum computationally achievable value of  $Re$ , namely about  $10^6$ . An alternative approach is to work ‘top-down.’ That is, to numerically simulate only the large-scale motions of the flow, down to the spatial resolution defined by the grid size  $\Delta$  in the computational domain. One can then introduce a turbulent eddy viscosity formalism to model the influence of the small-scale motions whose size is less than  $\Delta$ . This approach, which is known as subgrid-scale [SGS] modelling, was first introduced by Smagorinsky (1963) in a landmark study of the general circulation of the Earth’s atmosphere. The method has a sound theoretic base and has been tested successfully in a wide variety of fluid dynamic and thermal convection applications (Deardorff 1971; Chan & Sofia 1986; Fox, Sofia, & Chan 1991).

### **3.2 The velocity-dependent turbulent viscosity $\nu_t$**

The SGS modelling technique works as follows. According to the Kolmogorov (1941) theory of 3D isotropic turbulence, molecular viscosity causes large-scale features of the flow to decay into small ones which, in turn, break down into even smaller ones until the Kolmogorov length scale  $l_K$  is attained. In terms of the Fourier wave number spectrum of specific kinetic energy, namely  $E(k, t)$ , where  $k$  is the wave number and  $t$  the local time, there is a progressive cascade of energy from small to large wave numbers  $k$ . When statistical equilibrium is attained, there exists an inertial subrange  $k \ll k_K$  for which  $E(k, t)$  is both independent of the viscosity  $\nu$  and scales as  $k^{-5/3}$  (Landahl & Mollo-Christensen 1992, p. 59). In that case, it should still be possible to faithfully model the large-scale features of the

system by choosing a much larger turbulent viscosity  $\nu_t$  such that the effective Reynolds number  $Re_t = (\nu/\nu_t) Re$  now lies within the capacity of the computer, namely  $Re_t \leq 10^6$ .

Smagorinsky (1963) related  $\nu_t$  to the deformation tensor

$$S_{ij} = \frac{1}{2} \left( \frac{\partial u_i}{\partial x_j} + \frac{\partial u_j}{\partial x_i} \right) \quad (3)$$

of the large-scale velocity field  $u_i$  ( $i = 1, 2$ ) according as

$$\nu_t = (C_v \Delta)^2 \sqrt{2S^2} \quad (4)$$

where  $S^2 = S_{ij}S_{ij}$ . Such a construction yields a long-term Fourier spectrum  $E(k)$  for the kinetic energy per unit mass  $\frac{1}{2}\mathbf{u}^2$  which, for a suitable choice of the dissipation constant  $C_v$ , exhibits the familiar Kolmogorov power law cascade at length scales comparable with the mean 2D grid size  $\Delta = (\Delta_x \Delta_y)^{1/2}$ . That is, the grid cutoff wave number  $k_c = L/\Delta$  lies within the inertial subrange (Lilly 1971; Deardorff 1971; Lesieur 1997). Now the constant  $C_v$  controls the kinetic energy dissipation rate. Choosing  $C_v = 0.4$ , the dissipation rate at  $k = k_c$  matches the energy injection rate at low wave numbers and  $E(k)$  follows the  $-5/3$  law. This value is appropriate to 2D studies of atmospheric circulation. A somewhat smaller value, viz  $C_v = 0.2$ , emerges from 3D studies (Deardorff 1971).

### 3.3 The turbulent thermal diffusivity $\kappa_t$

It remains to specify the thermal diffusivity  $\kappa$ . Now as the Peclet number  $Pe = LU/\kappa$  in a stellar atmosphere is also extremely large if  $\kappa$  is derived from molecular processes (de Loore

1970), it is again necessary to adopt an SGS eddy formalism to model the transfer of heat to the subgrid length scales. Following Chan et al. (1982) and Chan & Sofia (1986), we adopt a turbulent thermal diffusivity  $\kappa_t$  having the same functional form as  $\nu_t$ . We have simply

$$\kappa_t = \nu_t / \sigma_t \quad (5)$$

where  $\sigma_t$  is the turbulent Prandtl number. This number is assumed to be a constant.

What little is known about the quantity  $\sigma_t$  is that  $\sigma_t < 1$ . This is because the thermal energy that is produced by the viscous dissipation of kinetic energy at short wavelengths needs to be re-injected back into the system at longer wavelengths in order to prevent a massive build-up of heat at the grid cutoff wavelength  $\lambda_c = \Delta$ . In fact, looking ahead to equation (12) in Section 4, we see that the heat diffusion term matches the viscous energy production term when the ratio of operating wavelengths is

$$\lambda_\kappa / \lambda_\nu \approx [\gamma / (\gamma - 1) \sigma_t]^{1/2} \quad (6)$$

The numerical investigations of Deardorff (1971) suggest that  $\sigma_t = 1/3$ . This gives  $\lambda_\kappa / \lambda_\nu \approx 3$ , noting that  $7/5 \leq \gamma \leq 5/3$ . This result was also confirmed by Dyt (1997) when carrying out test simulations of thermal convection in the protosolar atmosphere. He found that if  $\sigma_t = 1/2$ , then the wavelengths at which thermal energy is injected back into the system as kinetic energy, via the action of buoyancy, lies too close to those from which kinetic energy is being removed by viscosity to prevent a build-up of energy at  $\lambda = \lambda_c$ . Such a system soon becomes numerically unstable. We therefore adopt the choice  $\sigma_t = 1/3$ .

## 4. EQUATIONS AND PARAMETERS OF THE MODEL ATMOSPHERE

### 4.1 The gas dynamic equations

The model atmosphere is a 2D section of an ideal gas layer which is bounded above and below by two horizontal and impenetrable edges that are separated by a vertical distance  $d$ . We let  $x$  and  $z$  denote Cartesian spatial coordinates with  $z$  measured downwards from 0 to  $d$ . The flow is assumed to be horizontally periodic over the distance  $Xd$ , where  $X = 4$  is the aspect ratio. This is chosen large enough so that the condition of periodicity does not introduce a spurious time dependence into the convective flow (Hurlburt et al. 1984).

The initial atmosphere is assumed to be stationary and to have a superadiabatic polytropic structure with temperature  $T_{\text{in}}$  and density  $\rho_{\text{in}}$  distributions given by the equations

$$T_{\text{in}}(x, z) = T_0 (1 + \theta z/d) \quad (7a)$$

$$\rho_{\text{in}}(x, z) = \rho_0 (1 + \theta z/d)^{m_{\text{in}}} \quad (7b)$$

Here  $T_0$  and  $\rho_0$  denote the temperature and density on the upper boundary ( $z = 0$ ) and  $\theta$  is a dimensionless parameter that defines the initial temperature gradient in the atmosphere. The initial gas pressure distribution is  $p_{\text{in}}(x, z) = \rho_{\text{in}} \mathcal{R} T_{\text{in}} / \mu$ . The atmosphere is subject to a uniform gravitational acceleration  $g$ , which is assumed to be directed vertically downwards along the axis  $Oz$ . The condition for hydrostatic equilibrium in the initial atmosphere yields

$$m_{\text{in}} + 1 = \mu g d / \mathcal{R} T_0 \theta \quad (8)$$

As long as  $m_{\text{in}} < (\gamma-1)^{-1}$ , where  $\gamma = c_p/c_v$  is the ratio of principal specific heats  $c_p$  and  $c_v$ , and  $c_p - c_v = \mathcal{R}/\mu$ , the atmosphere is thermally unstable. Convective motion then quickly ensues provided that the Rayleigh number  $Ra$  exceeds a critical value  $\sim 660$  needed to overcome viscous resistance and thermal diffusive loss (cf. Gough et al. 1976).

We now choose the layer thickness  $d$  as the unit of length and  $t_0 = d/\sqrt{\mathcal{R}T_0/\mu}$  as the unit of time. This quantity is the isothermal sound crossing time evaluated at the top boundary ( $z=0$ ). Next, we define  $x_1 = x/d$  and  $x_2 = z/d$  to be the dimensionless spatial Cartesian coordinates and  $u_1$  and  $u_2$  to be the corresponding dimensionless velocities of the flow, expressed in units of the top boundary isothermal sound speed  $v_0 = \sqrt{\mathcal{R}T_0/\mu}$ . If  $\rho$ ,  $T$ , and  $p$  denote the dimensionless density, temperature and pressure, expressed in units of  $\rho_0$ ,  $T_0$  and  $p_0 = \rho_0 \mathcal{R}T_0/\mu$ , the set of dimensionless tensor equations which control the convection are

$$\text{Conservation of mass:} \quad \frac{\partial \rho}{\partial t} = -\frac{\partial}{\partial x_j}(\rho u_j) \quad (9)$$

*Conservation of momentum* ( $i = 1, 2$ ):

$$\frac{\partial}{\partial t}(\rho u_i) = -\frac{\partial}{\partial x_j}(\rho u_i u_j) - \frac{\partial p}{\partial x_i} + \frac{\partial}{\partial x_j}(\rho \nu_i \sigma_{ij}) + (m_{\text{in}} + 1)\theta \rho \delta_{i2} \quad (10)$$

$$\text{where} \quad \sigma_{ij} = \frac{\partial u_i}{\partial x_j} + \frac{\partial u_j}{\partial x_i} - \frac{2}{3}\delta_{ij} \frac{\partial u_k}{\partial x_k} \quad (11)$$

*Conservation of energy:*

$$\frac{\partial E_s}{\partial t} = -\frac{\partial}{\partial x_j}(E_s + p)u_j + \left(\frac{\gamma}{\gamma-1}\right) \frac{\partial}{\partial x_j} \left( \rho \kappa_i \frac{\partial T}{\partial x_j} \right) + \frac{\partial}{\partial x_j}(\rho \nu_i \sigma_{ij} u_i) + (m_{\text{in}} + 1)\theta \rho u_2 \quad (12)$$

$$\text{where} \quad E_s = \frac{1}{2} \rho u_i u_i + p/(\gamma-1) \quad (13)$$

*Perfect gas equation of state:*  $p = \rho T$  (14)

This set of equations enables us to solve uniquely for  $\rho$ ,  $T$ ,  $p$ ,  $u_1$ ,  $u_2$ , and the stagnation energy  $E_s$ . The solution is controlled by the parameters  $m$ ,  $\theta$ , and  $\gamma$ . The turbulent kinematic viscosity  $\nu_t$  and turbulent diffusivity  $\kappa_t$  are defined in Section 3.

## 4.2 The boundary conditions

To complete the statement of the mathematical problem, it is necessary to specify the boundary conditions. These are the same as the ones chosen by Cattaneo et al. (1990, 1991) and Dyt & Prentice (1998), namely

$$u_2 = 0 \text{ and } \partial u_1 / \partial x_2 = 0 \text{ at } x_2 = 0, 1 \quad (15a)$$

$$T = 1 \text{ at } x_2 = 0, \partial T / \partial x_2 = \theta \text{ at } x_2 = 1 \quad (15b)$$

The constraints on the velocity components  $u_1$  and  $u_2$  follow directly from the assumed stress-free and impenetrable nature of the upper and lower boundaries. The condition of fixed temperature gradient  $\theta$  at the lower boundary models a system where there is an assumed steady injection of heat into the base of the atmosphere. The condition of constant temperature  $T = 1$  at the top boundary requires some physical justification. First, it is the one that has been adopted by the Cattaneo group. The Chan group has adopted a very similar condition, namely one of constant entropy, at the top boundary. Second, in the case of the protosolar or protoplanetary clouds (Prentice 1978b, 2001a), the photosurface defines the upper boundary of the convective zone. It is from this level that all of the heat generated



through the gravitational contraction of the deep interior of the cloud can be finally radiated freely into space. But the radiative flux  $L \propto T_{\text{ph}}^4$  depends directly on the photosurface temperature  $T_{\text{ph}}$  and not on the outward temperature gradient  $\partial T/\partial z$ . In modelling the outer convective zone of a protosolar or protoplanetary cloud of, say, given luminosity, it is appropriate, therefore, that we choose the condition of constant temperature at the upper boundary.

In the present work we have ignored the contribution of radiation in the heat transfer process in the model atmosphere. This may possibly be a reasonable approximation since the radiative conductivity  $\kappa_{\text{rad}} \propto T^3/\rho$  becomes small relative to the turbulent conductivity  $\kappa_t$  in the upper levels of a convective stellar atmosphere (cf. Fox et al. 1991). Next, it is true that for main sequence stars and high temperature stellar objects, magnetic forces exert a dominant influence on the energy transfer mechanism at the photo-surface. But for the protosolar cloud—and especially for the clouds that formed Jupiter and Saturn—the surface temperatures are quite low (typically  $T_{\text{ph}} \lesssim 2000$  K). Ionization levels are thus also low and indeed negligible throughout the cloud’s interior during the early stages of its gravitational contraction from the orbit of Neptune (Prentice 1978a, b). Magnetic phenomena can thus be safely ignored in the present study.

## 5. THE NUMERICAL SCHEME

### 5.1 The flux-corrected transport scheme

The partial differential equations (9), (10), and (12) are solved numerically using a flux-corrected transport scheme that was originally devised by Boris & Book (1973) and improved later by Zalesak (1979). The Zalesak flux-corrected transport scheme (hereafter ZFCT) provides a means for accurately solving the equations of gas dynamics when steep gradients and shocks are encountered. Such features are a characteristic of supersonic flow. Unfortunately, they are also a source of numerical error in the solution. The error is generated in the treatment of the advective components  $\partial(Qu_j)/\partial x_j$  of the partial differential equation. Here  $Q$  denotes a physical quantity of the flow, such as the gas density  $\rho$ . Although computational schemes of first-order in spatial accuracy are stable in regions of rapid change, they yield solutions that suffer from severe numerical diffusion. Higher-order schemes are able to preserve the height and width of any modelled impulse, but produce unphysical oscillations in its bow and wake. ZFCT operates by combining the schemes of first and higher order in a manner which both restores diffusive loss and corrects for any unphysical ripples. A more detailed description of how the scheme operates is given in Dyt & Prentice (1998).

### 5.2 Specifying the computational domain

The two-dimensional model atmosphere consists of  $200 \times 50$  uniformly-spaced rectangular cells whose sides are aligned with the coordinate axes  $Ox$  and  $Oz$ , respectively. The physical dimensions of the sides are  $\Delta_x = Xd/200 = 0.02d$  and  $\Delta_z = 0.02d$ . The centre point of each

cell is denoted by  $(x_i, z_j)$  with  $i = 1, 2, \dots, 200$  and  $j = 1, 2, \dots, 50$ . All physical quantities  $Q$  are computed at the centre position of each cell  $(i, j)$  and the values denoted by  $Q_{i,j}$ . The initial polytropic atmosphere is defined by equations (7a) and (7b) with polytropic index  $m_{\text{in}} = 1$  and dimensionless temperature gradient  $\theta = 10$ . These are the values chosen by Cattaneo et al. (1990, 1991). The initial temperature contrast  $T_1/T_0$  between the base ( $x_2 = 1$ ) and top ( $x_2 = 0$ ) boundaries is thus  $T_1/T_0 = 1 + \theta = 11$ . Since the ratio of specific heats is  $\gamma = 1.4$ , the choice  $m_{\text{in}} = 1$  ensures that the atmosphere is everywhere strongly superadiabatic prior to the onset of convection.

## 6. RESULTS: FLOW STRUCTURE AND ENERGY FLUXES

### 6.1 Early stages of the convection

A small perturbation of temperature is introduced at several cell points near the top of the initially stationary atmosphere. After time  $t = 2$  units, where the unit is  $t_0$  as defined in Section 4, the buoyancy-driven disturbance has propagated through the entire computational domain. The velocity flows are everywhere small and chaotic. The horizontally averaged temperature and density distributions, namely  $\bar{T}(z, t)$  and  $\bar{\rho}(z, t)$  hardly differ from the initial profiles defined by equations (7a) and (7b). By time  $t = 4$ , however, the velocity field begins to take on a less chaotic pattern with the emergence of two well-defined horizontal pairs of giant convective cells of opposing circulation. These cells span the full depth of the atmosphere.

At this stage the vertical gradient  $\partial\bar{T}/\partial z$  of the horizontally-averaged temperature profile begins to flatten off in the lower 90 percent of the atmospheric depth. This leveling off is due to the strong, spatially-concentrated downdraft of cold, low-entropy gas which forms at the top boundary. The descent of this cold gas destroys the excess superadiabaticity of the lower atmosphere. The bottom 25 percent of depth actually becomes progressively subadiabatic, with the horizontally-averaged polytropic index  $\bar{m}(z,t) \equiv \partial(\ln \bar{\rho})/\partial(\ln \bar{T})$  exceeding the adiabatic value  $m_{\text{ad}} = 2.5$  everywhere except as  $z \rightarrow d$ , where  $\bar{m}(d,t) = 1$  because of the imposed temperature gradient given by equation (15b). In stark contrast with the circumstances in the lower atmosphere, the mean temperature gradient in the upper 10 percent of depth steepens up. At time  $t = 4$ ,  $\partial\bar{T}/\partial z$  at  $z = 0$  is about 5 times the initial dimensionless slope [ $\theta = 10$ ]. This implies a dramatic increase of superadiabaticity in those parts. In fact the increase is so great that the mean polytropic index  $\bar{m}(z,t)$  actually becomes negative.

## 6.2 The long-term, quasi-equilibrium state

As time progresses, the random nature of the early, large-scale velocity field disappears, and the convective flow becomes more settled. By time  $t = 10$ , the system has achieved a stable, quasi-equilibrium state, judged by when the ratio of the total heat flux at the top boundary ( $F_{\text{top}}$ ) to that at the base ( $F_{\text{base}}$ ) remains close to unity. The total heat flux  $F_{\text{tot}}(z)$  at depth  $z$  and its various components are defined in Section 6.3. At the top and bottom boundaries all heat transfer occurs via thermal diffusion. Fig. 1 shows a plot of  $F_{\text{top}}$ ,  $F_{\text{base}}$  and  $F_{\text{top}}/F_{\text{base}}$  as a function of time  $t$ . Unlike the numerical simulations of Hurlburt et al. (1984) and Cattaneo et

al. (1990, 1991), the heat flux at the base of the atmosphere, namely  $F_{\text{base}} \propto \overline{\rho \kappa_1 \partial T / \partial z}|_{z=d}$ , is not constant. This is because the thermal diffusivity  $\kappa_1$  now depends on the velocity field, which remains unsteady. The same is true for the diffusive heat flux at the top, namely  $F_{\text{top}} \propto \overline{\rho \kappa_1 \partial T / \partial z}|_{z=0}$ . Thus by time  $t \simeq 10$ , the ratio  $F_{\text{top}}/F_{\text{base}}$  reaches unity. Thereafter this ratio fluctuates randomly about this mean by  $\pm 15$  percent over a time scale of about 10 units. We may describe this behaviour as the evolved, long-term turbulent state of the system.

Fig. 2 shows the contours in the  $(x_1, x_2)$  plane of constant temperature  $T(x_1, x_2, t)$  and density  $\rho(x_1, x_2, t)$  along with the flow lines of the velocity field, all at time  $t = 60$ . Most notable in these diagrams is the existence of an extremely strong downflow of cold, dense gas near  $x_1 = 1.3$ . Here the temperature contours take a sharp downward dip while the density contours shift upwards indicating the presence of very dense gas at the head of the downflow. Near  $x_1 = 3.8$  there is a corresponding broad updraft of warm, light gas. But the departures  $T'(x_1, x_2, t)$  and  $\rho'(x_1, x_2, t)$  of temperature and density from the local horizontal averages  $\bar{T}(x_2, t)$  and  $\bar{\rho}(x_2, t)$  are here quite small compared to those present in the spatially concentrated downflow at  $x_1 = 1.3$ . The peak downflow speed  $w$  at  $x_1 = 1.3$  is 2.8 times the isothermal sound speed unit  $v_0$ , computed at the top boundary. It occurs at depth  $x_2 = 0.55$  and has local adiabatic Mach number  $M = w/v_{\text{ad}} = 1.08$ . The peak upflow speed occurs at  $x_1 = 3.8$  is  $2.0v_0$ . It occurs at depth  $x_2 = 0.65$  and has  $M = 0.65$ . Overall, the convective speeds obtained in this simulation are quite modest. Supersonic speeds are attained only in the rapid downflows at mid-depths and in parts of the horizontal flow near the top boundary.

### 6.3 Energy transfer through the atmosphere

Consider now the variation with depth  $z$  of the horizontally-averaged vertical fluxes of kinetic energy  $F_{\text{ke}}(z)$ , enthalpy  $F_{\text{ep}}(z)$ , heat diffusion  $F_{\text{diff}}(z)$ , and viscous dissipation  $F_{\text{diss}}(z)$ .

If  $u$  and  $w$  denote the horizontal and vertical components of the physical velocity vector  $\mathbf{u}(x, z, t)$ , then the fluxes are defined

$$F_{\text{ke}}(z) = \frac{1}{2} \overline{\rho u^2 w} \equiv \frac{1}{4d} \int_0^{4d} \rho u^2 w dx \quad (16)$$

$$F_{\text{ep}}(z) = c_p \overline{\rho T' w} \equiv \left( \frac{\gamma}{\gamma - 1} \right) \frac{\Re}{4\mu d} \int_0^{4d} \rho T' w dx \quad (17)$$

$$F_{\text{diff}}(z) = c_p \overline{\rho \kappa_t \frac{\partial T}{\partial z}} \quad (18)$$

$$F_{\text{visc}}(z) = \overline{\rho \nu_t \left( u \frac{\partial u}{\partial z} + \frac{4w}{3} \frac{\partial w}{\partial z} + u \frac{\partial w}{\partial x} - \frac{2w}{3} \frac{\partial u}{\partial x} \right)} \quad (19)$$

The expression for  $F_{\text{ep}}$  has been simplified by exploiting the equilibrium mass conservation equation  $\overline{\rho w} = 0$ . The total flux of energy transported across each horizontal plane is

$$F_{\text{tot}} = F_{\text{ke}} + F_{\text{ep}} + F_{\text{diff}} + F_{\text{visc}} \quad (20)$$

Fig. 3 shows the run with dimensionless depth  $z/d$  of the various energy fluxes expressed in units of  $\rho_0 [\Re T_0 / \mu]^{3/2}$  at time  $t = 60$ . Fig. 4 shows the individual dimensionless kinetic energy flux components  $F_{\text{ke}}(i, j)$  and those of the enthalpy flux  $F_{\text{ep}}(i, j)$  at each grid point  $(i, j)$  in the modelled zone, plotted against the vertical component  $w$  of velocity expressed in units  $v_0$ . Looking at Fig. 4, we see that  $F_{\text{ke}}(i, j)$  has a cubic distribution. This result, which was also

found by Cattaneo et al. (1991), is to be expected, especially for the higher values of  $w$  since the velocity vector  $\mathbf{u}$  is directed principally along the  $Oz$  axis, giving  $|\mathbf{u}|^2 \simeq w^2$  and hence  $F_{ke} \simeq \frac{1}{2} \rho w^3$ . For lower values of  $w$ , say for  $|w| \lesssim 1.5v_0$ , the upward and downward components of the kinetic energy flux cancel each other, giving no net flux. This result concurs with the conventional mixing length of convection.

The symmetry between the strengths of the upflows and downflows breaks down for the higher values of vertical velocity  $w$ . As a result, there is a net downward (positive) flux of kinetic energy at each depth  $z$  as seen in Fig. 3. Much of the net downflux of kinetic energy and also the net upward flux of enthalpy is due to the very strong downflow current near  $x_1 \simeq 1.3$ . The origin of this upflow/downflow asymmetry, which is also present in the numerical simulations of Hurlburt et al. (1984), Chan & Sofia (1989), Cattaneo et al. (1990, 1991) and Dyt & Prentice (1998), may be traced to the condition of fixed temperature  $T = T_0$  at the top boundary. This condition ensures a steady supply of cold, negatively buoyant gas at the head of each downflow. At the lower boundary ( $z = d$ ), however, the temperature is not fixed. Thus the destruction of the superadiabatic structure of the lower atmosphere by the descending low entropy gas means that warm rising gas enjoys only weak upward buoyancy.

Next, we note that except near the upper and lower boundaries, the bulk of the energy transfer through the atmosphere is facilitated principally by convective motion (i.e., by  $F_{ke}(z)$  and  $F_{ep}(z)$ ) rather than by diffusive exchange ( $F_{diff}$ ). We also note that in the upper 50 percent of the atmosphere the enthalpic flux is by far the largest of the three convective fluxes  $F_{ke}$ ,

$F_{\text{ep}}$ , and  $F_{\text{visc}}$ . This is so since the downflow of very cool gas at  $x_1 \simeq 1.3$  has not achieved full speed. Also  $F_{\text{ep}}$  is everywhere much larger than  $F_{\text{diff}}$ , except near the boundaries. The viscous heating flux  $F_{\text{visc}}$  is mostly negligible everywhere, except near the boundaries. At the top and bottom boundaries, all vertical motion ceases (i.e.,  $w = 0$ ) so each of  $F_{\text{ke}}$ ,  $F_{\text{ep}}$ , and  $F_{\text{visc}}$  are zero there.

Diffusion is the sole energy transfer mechanism at the boundaries  $z = 0$  and  $z = d$ . It also plays an important role in part of the deep atmosphere near  $z \approx 0.8d$ , where  $F_{\text{ke}}$  and  $F_{\text{ep}}$  nearly cancel each other out. Here  $F_{\text{diff}}$  is comparable with the size of the total convective flux  $F_{\text{conv}} = F_{\text{ke}} + F_{\text{ep}} + F_{\text{visc}}$ . For most of the atmospheric interior, however, large-scale convection is the main energy transfer mechanism.

Consider next Fig. 5, which shows the variation of the various energy flux components with horizontal distance  $x/d$  at time  $t = 60$ . Spatial averaging is now performed in the vertical direction yielding the quantities  $F_{\text{ke},v}(x)$ ,  $F_{\text{ep},v}(x)$ ,  $F_{\text{diff},v}(x)$ , and  $F_{\text{visc},v}(x)$ . Thus,  $F_{\text{ke},v}(x) = \frac{1}{d} \int_0^d \frac{1}{2} \rho u^2 w dz$ , etc. The unit of flux is  $\rho_0 [\Re T_0 / \mu]^{3/2}$  as before. We see that the kinetic energy flux  $F_{\text{ke},v}(x)$  and enthalpy flux are strongly correlated, as is to be expected. Thus, the very strong positive downflux of kinetic energy at  $x_1 = 1.3$  is accompanied by an equally strong but oppositely directed flux of enthalpy. The descending gas is, of course, much cooler than the mean surroundings so  $F_{\text{ep},v} < 0$ . The two fluxes  $F_{\text{ke},v}$  and  $F_{\text{ep},v}$  effectively cancel each other out in this downflow. At  $x_1 \simeq 3.8$ , however, there is a weak upflow of gas that is slightly warmer than the mean surroundings. Here the two fluxes  $F_{\text{ke},v}$



and  $F_{\text{ep},v}$  work together to yield a net upflow of energy in that section of the atmosphere. Cattaneo et al. (1991) also observed that it is the weaker components of convection which contribute most to the net transfer of heat through the atmosphere. The very strong components simply serve to redistribute the various energy ingredients around the atmosphere, so creating a large reservoir of mechanical energy.

#### 6.4 Comparison with a previous simulation

The picture presented here differs significantly from the one found earlier by Dyt & Prentice (1998). In this previous simulation, heat diffusion was mostly facilitated by a velocity-independent thermal diffusivity. Diffusion controlled most of the heat transfer through the atmosphere. In the present simulation, the thermal diffusivity  $\kappa_i$  is derived via a subgrid-scale eddy formalism. It depends on the velocity field  $u_i$  and, in particular, is proportional to the magnitude of the various gradients  $|\partial u_i / \partial u_j|$  as described in Section 3. These gradients are generally smaller in the middle atmosphere and far from the boundaries. In these parts, thermal diffusion is thus a minor carrier of energy compared to the convective mechanisms.

Another principal difference between the present simulation and that of Dyt & Prentice (1998) is the unsteady character of all those physical quantities which depend directly on the velocity field  $u_i$ . This is especially apparent for the energy fluxes. Not only does the ratio of the total flux leaving the top of the atmosphere to that at the base, namely  $F_{\text{top}}/F_{\text{base}}$ , remain unsteady with time, as seen in Fig. 1, but the total flux at each depth is also time dependent. Cattaneo et al. (1991) have also reported the unsteady character of the convection in the

regime of low Prandtl number, or viscosity, when the flow is highly turbulent. They find that ‘there can be fluctuations in the values of the horizontally-averaged fluxes of up to 30 percent.’ In the present simulation the unsteady behaviour of the energy fluxes is most likely due to the fact that the turbulent viscosity and thermal diffusivity are velocity dependent. This renders the system of equations for the thermal evolution of the atmosphere extremely non-linear. The solution is now much more complex and prone to instability. The convection thus exhibits turbulence.

## 7. RESULTS: THE LONG-TERM PHYSICAL STRUCTURE AND TURBULENT STATE OF THE ATMOSPHERE

### 7.1 The long-term mean profiles of temperature, density, and pressure

Consider now Figs. 6, 7, and 8 which show the run of the horizontally-averaged temperature  $\bar{T}(z,t)$ , density  $\bar{\rho}(z,t)$ , and pressure  $\bar{p}(z,t)$  with depth  $z$  at time  $t = 60$ . As noted in Section 6.1, the very strong downdraft of low entropy gas profoundly influences the thermal structure of the lower atmosphere. The descent of this cold gas destroys much of the superadiabatic excess of the lower region and flattens the temperature profile with increasing depth. The initial quiescent atmosphere has a uniform polytropic index  $\bar{m}(z,0) = \partial(\ln \bar{\rho}) / \partial(\ln \bar{T}) = 1$ . For the evolved atmosphere,  $\bar{m}(z,60)$  rises sharply from 1 to the adiabatic value  $\bar{m}_{\text{ad}} = 2.5$  as  $z$  goes from  $0.1d$  to  $0.2d$ . It then remains bounded between 1.5 and 2.5 on the interval  $0.2d \leq z \leq 0.75d$ , with a mean of 2. At  $z = 0.75d$ , the gas becomes adiabatically neutral again, with  $\bar{m}(0.75d,60) \simeq 2.5$ . This is evidenced in the velocity flowline diagram in Fig. 2 which shows pockets of gas that are neither moving up or down from this level.

For  $z > 0.75d$ ,  $\bar{m}(z,60)$  increases sharply with depth so that the bottom 25 percent of the atmosphere is actually rendered subadiabatic by the powerful downdraft of gas at  $x = 1.3d$ . Superadiabaticity returns only at  $z = d$  due to the imposed temperature gradient, given by equation (15b). This provides the heat flow into the base of the atmosphere. Rising updrafts which form near the base thus enjoy very limited opportunity for buoyant lift compared to the favourable conditions available to the downdrafts at  $z = 0$ . This result is a sustained feature of the evolved convective flow. That is, the horizontally-averaged profiles  $\bar{T}(z,t)$ ,  $\bar{\rho}(z,t)$ , and  $\bar{p}(z,t)$  exhibit very little time dependence, despite the large temporal fluctuations of the convective fluxes, as mentioned in Section 6.4. The average difference in  $\bar{T}(z,t)$  between  $t = 54$  and  $t = 60$ , for example, is less than 1 percent at all depths.

Another important feature to notice in Fig. 6 is that in the upper 10 percent of the atmosphere, and especially in the top 5 percent of its height, the horizontally-averaged temperature gradient  $\partial\bar{T}/\partial z$  actually steepens up and exceeds the initial, superadiabatic gradient  $\theta = 10$  by a factor of about 3. For  $z < 0.1d$ , the local polytropic index  $\bar{m}(z,60) < m_{in} = 1$ . For  $z \lesssim 0.07d$ ,  $\bar{m}(z,60) < 0$  and at  $z = 0$ ,  $\bar{m}(0,60) = -0.65$ . The upper 7 percent of the atmosphere is thus so convectively unstable that a steep density inversion takes place. This unanticipated but extremely important discovery is clearly observed in Fig. 7. The mean density  $\bar{\rho}(z,60)$  rises a factor 3.5 times the initial physical value  $\rho_0$  at  $z = 0$ .

## 7.2 Origin of the steepened temperature gradient and density inversion at the top of the atmosphere

The greatly steepened temperature gradient and density inversion at the top of the model atmosphere are due to the fact that the turbulent diffusive flux  $F_{\text{diff}}$  is directly proportional to the gas density  $\rho$ . At the top and bottom boundaries, all of the convective fluxes are zero since  $w = 0$ . The energy transfer at these levels is achieved solely by diffusion. We have also seen that the convection fluctuates about a long term [lt] quasi-equilibrium state defined by the energy balance equation  $\overline{\rho_{\text{lt}} \kappa_t (dT_{\text{lt}}/dz)} \Big|_{z=0} = (T_0 \theta/d) \overline{\rho_{\text{lt}} \kappa_t} \Big|_{z=d}$ , noting that the mean temperature gradient at the base is constrained to match the value  $T_0 \theta/d$  by virtue of the boundary condition there (equation 15(b)). Here  $\overline{\rho_{\text{lt}}}(z)$  is the long-term average of  $\overline{\rho}(z,t)$ . It differs from  $\overline{\rho}(z,60)$  by < 1 percent.  $\overline{T_{\text{lt}}}(z) \simeq \overline{T}(z,60)$  is the long-term average temperature at depth  $z$ . Now the turbulent diffusivity  $\kappa_t$  is proportional to the magnitude  $S$  of the velocity deformation tensor  $S_{ij}$  defined in Section 3. On the boundaries  $S = [(\partial u/\partial x)^2 + (\partial w/\partial z)^2]^{1/2}$ . This quantity has a similar mean value  $\overline{S}$  at  $z = 0$  as at  $z = d$ , to within a factor of 2. With fair approximation therefore, returning to physical units, we have

$$\left. \frac{d\overline{T_{\text{lt}}}}{dz} \right|_{z=0} \approx (T_0 \theta/d) \overline{\rho_{\text{lt}}}(d) / \overline{\rho_{\text{lt}}}(0) \quad (21)$$

Hence as the density at the top boundary  $\overline{\rho_{\text{lt}}}(0)$  is always much less than that at the base, namely,  $\overline{\rho_{\text{lt}}}(d)$ , it follows that  $d\overline{T_{\text{lt}}}/dz|_{z=0} \gg T_0 \theta/d$ . This accounts for the steepening of the temperature gradient near the top boundary.

Next consider the ideal gas equation  $p = \rho \mathcal{R} T / \mu$ . Applying horizontal averages, the numerical simulation yields  $\bar{p}_t \approx \bar{\rho}_t \mathcal{R} \bar{T}_t / \mu$  to within 0.5 percent of accuracy at each level  $z$ . Differentiating with respect to  $z$ , we have

$$\bar{T}_t d\bar{\rho}_t/dz \approx (\mu/\mathcal{R}) d\bar{p}_t/dz - \bar{\rho}_t d\bar{T}_t/dz \quad (22)$$

Hence if  $d\bar{T}_t(z)/dz$  is sufficiently large then  $d\bar{\rho}_t(z)/dz < 0$  and a density upturn occurs. Now the vertical gradient of the mean pressure  $\bar{p}_t(z)$  is mostly controlled by gravitational stratification and less so by the influence of convective motion. This is seen in Fig. 8, which shows the run of mean pressure  $\bar{p}$  with depth for both the initial and evolved atmospheres. The slopes are everywhere similar. In fact, it follows readily from equation (10) that by setting  $\partial/\partial t = 0$  and applying horizontal averaging, as well as using equation (15a) and ignoring viscous stress, that

$$\left. \frac{d\bar{p}_t(z)}{dz} \right|_{z=0} \approx (\mathcal{R} T_0 / \mu d) (1 + m_{\text{in}}) \theta \bar{\rho}_t(0) \quad (23)$$

Since  $\bar{T}_t(0) = T_0$ , it now follows from equations (21) and (22) that

$$\left. \frac{d\bar{\rho}_t(z)}{dz} \right|_{z=0} \approx [1 + m_{\text{in}} - \bar{\rho}_t(d)/\bar{\rho}_t(0)] \theta \bar{\rho}_t(0) / d \quad (24)$$

For the given choice of parameters  $m_{\text{in}} = 1$ ,  $\theta = 10$ , we have  $\bar{\rho}(d, 60) = 14.7 \rho_0$ ,  $\bar{\rho}(0, 60) = 3.5 \rho_0$ , and so  $d\bar{\rho}_t(z)/dz|_{z=0} \approx -77 \rho_0/d$  from equation (24). This value compares very well with the actual density gradient  $\partial \bar{\rho}(z, 60) / \partial z|_{z=0} = -78 \rho_0/d$  given by the numerical simulation at time  $t = 60$ .

### 7.3 The wave number spectrum of kinetic energy

Lastly consider Figure 9 which shows the globally-averaged, Fourier wave number spectrum  $\langle E(k_1, k_2) \rangle$  of the kinetic energy per unit mass  $\frac{1}{2} \mathbf{u}^2(i, j)$  plotted as a function of the horizontal wave number  $k_1 = 1, 2, 3, \dots, 200$  for four vertical wave numbers  $k_2 = 1, 8, 22$ , and  $43$  in the integer domain  $1, 2, 3, \dots, 50$  at time  $t = 60$ . Recalling that the two-dimensional model atmosphere consists of  $N \times M$  Cartesian gridpoints  $(i, j)$  where  $N = 200$  and  $M = 50$ , we define

$$e_{I,J}(i, j) = \frac{1}{2} \mathbf{u}(I, J) \cdot \mathbf{u}(I + i, J + j) \quad (25)$$

$$E_{I,J}(k_1, k_2) = \sum_{i=1}^N \sum_{j=1}^M e_{I,J}(i, j) \sin\left(\frac{2\pi k_1 i}{N}\right) \sin\left(\frac{2\pi k_2 j}{M}\right) \quad (26)$$

and

$$\langle E(k_1, k_2) \rangle = \frac{1}{NM} \sum_{I=1}^N \sum_{J=1}^M E_{I,J}(k_1, k_2) \quad (27)$$

The function  $\langle E(k_1, k_2) \rangle$  is the discrete Fourier sine transform of the spatial covariance of velocity, averaged over the whole atmosphere.

Now according to the Kolmogorov (1941) theory of stationary isotropic turbulence, the function  $\langle E(k_1, k_2) \rangle$  should exhibit the power law behaviour  $\langle E \rangle \propto k^{-5/3}$  for total wave number  $k = \sqrt{k_1^2 + k_2^2} \gg k_{\text{peak}}$ . Here  $k_{\text{peak}}$  is the wave number where the bulk of the energy resides and  $\langle E \rangle$  peaks (Landahl & Mollo-Christensen 1992, p. 59). Because the atmosphere is vertically stratified, it is not clear that the conditions of local isotropy are satisfied in the  $Oz$  direction except at places where the vertical grid size  $\Delta_2 = d/M$  is much smaller than the local pressure scale height  $h_2 = p/(\partial p/\partial z)$  (cf. Chan & Sofia 1986). For the initial atmosphere, we have

$\Delta_2/h_2 = 2\theta/(1 + \theta z/d)M$ . Since  $\theta = 10$  and  $M = 50$ , the condition for isotropy is easily met at the base of the atmosphere ( $z = d$ ) but barely so at the top. Fortunately, this condition is easily satisfied at all scales in the horizontal direction. We therefore expect  $\langle E(k_1, k_2) \rangle$  to exhibit the Kolmogorov power law dependence  $\langle E \rangle \propto k_1^{-5/3}$  with respect to  $k_1$  for all  $k_1 \gg k_{\text{peak}}$  and  $k_2 \gg k_{\text{peak}}$  provided that  $k_1^2 \gg k_2^2$  also, so that  $\sqrt{k_1^2 + k_2^2} \approx k_1$ .

Inspecting Fig. 9, we observe that the maximum value of  $\langle E(k_1, k_2) \rangle$  for each fixed  $k_2$  occurs at  $k_1 = 3$ . That is,  $k_{\text{peak}} \simeq 3$ . The same value  $k_{\text{peak}} \simeq 3$  applies to the distribution of  $\langle E \rangle$  with respect to  $k_2$  though the profile for  $k_2 = 3$  is not shown. In any event, we see that  $\langle E(k_1, k_2) \rangle$  diminishes rapidly for both  $k_1 \gg k_{\text{peak}}$  and  $k_2 \gg k_{\text{peak}}$ . Furthermore, for those sections of the curves for  $k_2 = 22$  and  $43$  where both of these inequalities are satisfied, and also  $k_1^2 \gg k_2^2$ ,  $\langle E(k_1, k_2) \rangle$  does scale as  $k_1^{-5/3}$ . That is, the wave number spectrum for the kinetic energy per unit mass, namely  $\frac{1}{2}u^2$ , does indeed exhibit the Kolmogorov power law expected for stationary isotropic turbulence.

We conclude that the Smagorinsky subgrid-scale formalism for dealing with the influence of turbulent motions whose length scale is smaller than the grid size  $\Delta$  has successfully worked in this numerical simulation. That is, the choices  $C_v = 0.4$  and  $\sigma_t = \frac{1}{3}$  for the Smagorinsky constant and turbulent Prandtl number, respectively, have resulted in a kinetic energy wave number spectrum  $\langle E(k_1, k_2) \rangle$  which displays the expected characteristics of stationary

turbulence for wave numbers  $k_1$  close to the cutoff value  $k_c = 200$ . That is,  $k_c$  appears to lie within an inertial subrange.

## 8. CONCLUSIONS AND DISCUSSION

### 8.1 Summary of main results

A computational scheme has been presented to numerically simulate the onset and evolution of turbulent, supersonic thermal convection in a 2D rectangular section of a gas layer. The layer is heated from below and stratified across many pressure scale heights by a uniform gravitational field. The purpose of this calculation is to reproduce the physical conditions in the outer layers of the protosolar cloud [PSC] in relation to the modern Laplacian theory of Solar System origin (the MLT—see Section 1). A constant temperature gradient  $\partial T/\partial z = T_0\theta/d$ , with  $\theta = 10$ , is maintained at the base  $z = d$ . Here  $T_0$  is the temperature on the top boundary ( $z = 0$ ), which is also kept fixed. This boundary corresponds to the photosurface level of the PSC. The initial run of density with temperature is superadiabatic, with polytropic index  $m_{\text{in}} = 1$ . The adiabatic index is 2.5, corresponding to a diatomic gas.

The present numerical simulation differs from the earlier one reported by Dyt & Prentice (1998) in that both viscous stress and thermal diffusion are now entirely modelled by the subgrid-scale turbulent eddy formalism due to Smagorinsky (1963). This procedure allows one to include the influence of all scales of the convective flow when the Reynolds number  $\text{Re} \simeq O(10^{12})$  associated with molecular diffusion greatly exceeds the largest Reynolds number  $\text{Re}_{\text{max}} \simeq O(L^2/\Delta^2) \sim 10^4\text{--}10^6$  of a flow that can be completely resolved on the



computational domain. Here  $L$  and  $\Delta$  are the lineal width and grid size of the domain. The large scale flow is solved for exactly using a flux-corrected transport technique due to Zalesak (1979). The influence of motions whose size is less than  $\Delta$  is accounted for with the use of the velocity-dependent turbulent viscosity  $\nu_t$  and thermal conductivity  $\kappa_t$  devised by Smagorinsky.

Convective motion sets in quickly and soon evolves to a quasi-equilibrium state. This state is attained when the diffusive heat flux at the top boundary, namely  $F_{\text{top}} = c_p \overline{\kappa_t \partial T / \partial z} \Big|_{z=0}$  first matches the heat flux entering the base, namely  $F_{\text{base}} = c_p \overline{\theta \rho \kappa_t} \Big|_{z=d}$ . The fluxes of kinetic energy, enthalpy, and viscous dissipation vanish on these boundaries because the vertical component  $u_2$  of velocity is zero there. Within the interior of the atmosphere, all of these convective fluxes as well as the diffusive flux are unsteady and vary by up to 30 percent after quasi-equilibrium is established. The convection is thus turbulent. The origin of the unsteadiness is due to the fact that  $\nu_t$  and  $\kappa_t$  are velocity dependent, so rendering the system of equations for momentum and energy balance to be extremely non-linear. Further evidence for the turbulent character of the large-scale flow comes the Fourier wave number spectrum of kinetic energy  $\langle E(k_1, k_2) \rangle$ . This exhibits the familiar Kolmogorov power law spectrum  $\langle E \rangle \propto k_1^{-5/3}$  for wave numbers  $k_1$  close to the horizontal grid cutoff value  $k_c = Xd/\Delta = 200$ , where  $Xd$  is the width of the atmosphere and  $X = 4$  is the aspect ratio for the simulation.

The long-term, large-scale convective flow consists of a row of adjacent pairs of giant convective cells of opposing circulation. Each cell pair spans the height of the atmospheric

layer. As also seen in Dyt & Prentice (1998), there is an asymmetry in the velocity and spatial structure of the upflows and downflows. The downflows are swift and narrow and consist of low entropy gas that is much denser than the mean surroundings. The peak downflow speed occurs at depth  $z \simeq 0.55d$  and has local adiabatic Mach number  $M \simeq 1.08$ . The upflows are broader and more sluggish and consist of gas that is barely warmer than the surroundings, as seen in Fig. 2. The peak upflow speed occurs at depth  $z = 0.65d$  where  $M \simeq 0.65$ . Overall, therefore, the maximum convective velocities found in this simulation are only just mildly supersonic.

The most important discovery of the present simulation is the steepening of the mean vertical temperature gradient  $d\bar{T}_t/dz$  at the top of the long-term atmosphere by a factor of about 3 times the initial dimensionless value  $\theta T_0/d$ , with  $\theta = 10$ . Correspondingly, there is an upturn of mean density  $\bar{\rho}_t(z)$  as  $z \rightarrow 0$ , with  $\bar{\rho}_t(0)$  being 3.5 times the initial density  $\rho_0$ . This situation comes about because the convective heat fluxes vanish at  $z = 0$  and  $z = d$ , and the thermal diffusive flux  $F_{\text{diff}} = c_p \rho \kappa_t \partial T / \partial z$  is proportional to the density  $\rho$ . Since  $\bar{\kappa}_t(z)$  has approximately the same value at  $z = 0$  as at  $z = d$ , long term energy balance dictates that  $d\bar{T}_t/dz|_{z=0} \approx (T_0/d)\theta \bar{\rho}_t(d)/\bar{\rho}_t(0)$ . Hence  $d\bar{T}_t/dz|_{z=0}$  greatly exceeds  $\theta T_0/d$ . It then follows from considerations of pressure balance that the sharp fall in  $\bar{T}_t(z)$  as  $z \rightarrow 0$  is accompanied by a sharp rise in  $\bar{\rho}_t(z)$ . In equation (24) we found that the strength of the density inversion is proportional to the imposed temperature gradient  $\theta$  at the base of the atmosphere.

## 8.2 Implications for the modern Laplacian theory

It remains to discuss the impact of these calculations on the modern Laplacian theory [MLT] of Solar System origin. Now in order for the MLT to be valid, it is necessary that two important criteria be satisfied. First, it is necessary that the mass distribution of the protosolar cloud [PSC] be very centrally condensed, thus allowing the contracting cloud to rid itself of excess spin angular momentum at the expense of losing very little mass. This helps explain the low mass of the planetary system relative to the Sun. Second, it is necessary that a very steep density inversion take place at the photosurface of the PSC, with the density rising 30–40 times the expected value for wholly adiabatic cloud structure of the same photosurface temperature  $T_0$  and density  $\rho_0$ . This enables the PSC to store above its photosurface 30–40 times more mass than expected. If such an event occurs, the contracting cloud proceeds to shed a discrete system of concentric gas rings whose orbital radii match the mean orbital spacings of the planets.

Previously it has been proposed that both of the above criteria may be solely achieved by the action of a radial turbulent stress  $\langle \rho_t v_t^2 \rangle$  arising from supersonic buoyant motions within the PSC. For a non-rotating cloud,  $\langle \rho_t v_t^2 \rangle = \beta \rho G M(r)/r$  where  $M(r)$  is the mass interior to radius  $r$  and  $\beta$  is a dimensionless constant (Prentice 1973). This non-thermal stress greatly expands the outer tenuous layers of the cloud, so lowering the axial moment-of-inertia factor  $f$ , as required. If  $\beta \sim 0.1$  then  $\langle \rho_t v_t^2 \rangle$  rises a factor  $P_{ph} \sim 30\text{--}40$  times the gas pressure  $\rho \mathcal{R}T/\mu$  just below the photosurface (Prentice 1996a, 2001a). The subsequent degeneration of all upward convective motion at the photosurface results in the formation of a dense lid of non-turbulent

gas. The density  $\rho_+$  of this lid at the photosurface exceeds that  $\rho_-$  of the fully turbulent gas just below it by the factor  $\rho_+/\rho_- = 1 + P_{\text{ph}} \sim 35$ , as required.

The problem with the model above, as stated in Section 2, is that such large turbulent stresses are unlikely to be achieved. They imply mean vertical convective velocities having Mach number  $M = \sqrt{P_{\text{ph}}/\gamma} \approx 5$ . Usually  $M \leq 2$ , though Cattaneo et al. (1990) have reported a peak  $M = 2.7$  in one numerical simulation. This implies a peak  $P_{\text{ph}} \simeq 10$ .

What has emerged from the numerical simulation reported here points a way forward for satisfying the criteria needed for the MLT without having to resort to unreasonably large convective velocities. First, as seen in Fig. 7 showing the run of the long term, horizontally-averaged density  $\bar{\rho}_{\text{lt}}(z)$  versus depth  $z$ , there is a net shift of mass towards the base of the model atmosphere. This corresponds to decrease in the axial moment-of-inertia factor of the PSC, as required by the MLT. Between  $z = 0.1d$  and  $z = 0.8d$ , the mean density  $\bar{\rho}_{\text{lt}}(z)$  of the long-term atmosphere is less than that of the initial quiescent atmosphere while as  $z \rightarrow d$ ,  $\bar{\rho}_{\text{lt}}(z)$  progressively exceeds  $\bar{\rho}_{\text{in}}(z)$ . The progressive compaction of the gas with increasing depth has, however, been brought on by the destruction of superadiabaticity through convective heat exchange, rather than through the action of vertical dynamical stress  $\langle \rho v_t^2 \rangle = \rho w^2$ , as proposed by Prentice (1973). Here  $w$  is the vertical component of physical velocity in the convective flow. As we saw in Fig. 2, the bulk of the flow is directed horizontally. The upflows and downflows each occupy only about 10 percent of the cross-sectional area of the model atmosphere at  $z = 0.5d$ . And the ratios  $P_t = \mu w^2/\mathcal{R}T$  of vertical

dynamical stress to gas pressure are both near their maximum values of 0.6 and 1.6, respectively. This yields a mean value  $\bar{P}_t \simeq 0.2$  at  $z = 0.5d$ . At  $z = 0.3d$ ,  $\bar{P}_t \simeq 0.1$ . At  $z = 0.1d$ , where the upflows and downflows occupy  $\sim 7.5$  percent and  $\sim 4.5$  percent of the cross-sectional area, and the  $P_t$  values are  $\sim 0.08$  and  $\sim 0.8$ , we have  $\bar{P}_t \simeq 0.04$ . Overall, therefore, the structure of the atmosphere is barely influenced by vertical dynamical stress in this simulation. It is superadiabaticity which has produced the most change.

As far as the second criterion of the MLT is concerned, we have found that there is indeed a sharp and significant density inversion at the top of the model atmosphere. The density  $\bar{\rho}_t(0)$  at  $z = 0$  is 1.8 times that at  $z = 0.07d$  and 3.5 times the density  $\rho_0$  at the top of the initial atmosphere. But again, this density increase has not come about as a result of turbulent stress. The small change in the value of  $\bar{P}_t$  from 0.04 to 0, as  $z$  passes from 0.1 to 0, contributes at most 4 percent of the 80 percent density increase between these levels. Instead the bulk of the density upturn is due to the dramatic increase in superadiabaticity as  $z \rightarrow 0$ . This has come about through the use of the subgrid-scale turbulence formalism to model the influence of convective motions whose scale is less than the computational grid size.

### 8.3 Finale

A picture of very strong thermal convection in a 2D model rectangular section of the outer layers of a non-rotating protosolar cloud has been presented. This model assists the validation of the MLT. Nonetheless, for the given choice of model parameters, especially for the initial dimensionless temperature gradient  $\theta = 10$ , the observed surface density increase factor

$\bar{\rho}_t(0)/\rho_0 = 3.5$  at the top boundary falls a long way short of the required value of 35. Now according to equation (24), the vertical gradient of the mean density  $\bar{\rho}_t(z)$  at  $z = 0$  is proportional to  $\theta$ . By suitably increasing  $\theta$ , therefore, it may be possible to achieve the desired density upturn factor of 35. Such an action will make the convection more vigorous, as follows.

From equation (10) it follows that the sum of the horizontally-averaged long-term pressure and dynamical stress satisfies the dimensionless equation  $\partial(\overline{\rho_t T_t} + \overline{\rho_t u_2^2})/\partial x_2 = (m_{in} + 1)\theta \bar{\rho}_t$ , ignoring horizontal gradients and viscosity. Hence we expect  $u_2^2$  and  $\overline{u_2^2}$  at any depth to scale in proportion with  $\theta$ . Increasing  $\theta$  by a factor  $\sim 7.5$ , say, may increase  $u_2^2$  everywhere by about the same factor. And as the temperature  $\bar{T}(z, t)$  is heavily constrained by the boundary conditions, and has the same value near  $z = 0.5d$  in both the initial and long term states, we expect that the peak value of  $P_t = u_2^2/T$  in the downflow, which also occurs at  $z \approx 0.5d$ , to increase from 1.6 to  $\sim 12$ . If the value of  $\bar{P}_t$  near  $z = 0.1d$ , where  $\bar{\rho}_t(z)$  is a minimum, also increases by the same factor of 7.5, then the density  $\bar{\rho}_t(0)$  at  $z = 0$  is increased by the factor  $\sim (7.5 \times 1.3) \approx 10$ . This yields an overall density upturn factor  $\bar{\rho}_t(0)/\rho_0 \approx 35$ , as needed. The peak Mach number for this realization is  $M_{\text{peak}} \approx 2.9$ , which is physically acceptable.

The suggestion that supersonic turbulent convection played an important role in the formation of the Solar System may thus be not such a far-fetched idea after all. Clearly many more numerical simulations are needed to determine whether all of the criteria required by the modern Laplacian theory can be met. The three-dimensional structure of the protosolar

cloud and the influence of rotation also need to be taken into account. The results reported here provide a very promising start.

## ACKNOWLEDGMENTS

AJRP thanks Dr. John D. Anderson [NASA/JPL] for his continued encouragement of this author's work and for generous financial support towards the production of this publication. CPD is grateful to the Australian Research Council for the funding of postgraduate research award. Thanks also are due to Mr. David Warren [Hobart] for additional funding, and to P. S. Cally and P. A. Fox for helpful discussions, and to C. R. Morgan, S. Morton, L. R. West, M. E. Young, J. M. Dedmon and R. V. Carlson for technical assistance.

## REFERENCES

- Boris J. P., Book D. L., 1973, "Flux-corrected transport. I. SHASTA, a fluid transport algorithm that works," *J. Comput. Phys.* **11**, 38–52.
- Cattaneo F., Brummell N. H., Toomre J., 1990, "Supersonic convection," *Astrophys. J.* **349**, L63–L66.
- Cattaneo F., Brummell N. H., Toomre J., Malagoli A., Hurburt N.E., 1991, "Turbulent compressible convection," *Astrophys. J.* **370**, 282–294.
- Chan K. L., Sofia S., Wolff C. L., 1982, "Turbulent compressible convection in a deep atmosphere. I. Preliminary two-dimensional results," *Astrophys. J.* **263**, 935–943.
- Chan K. L., Sofia S., 1986, "Turbulent compressible convection in a deep atmosphere. III. Tests on the validity of the numerical approach," *Astrophys. J.* **307**, 222–241.

- Chan K. L., Sofia S., 1989, "Turbulent compressible convection in a deep atmosphere. IV. Results of three-dimensional computations," *Astrophys. J.* **336**, 1022–1040.
- Deardorff J. W., 1971, "On the magnitude of the subgrid scale eddy coefficient," *J. Comput. Phys.* **7**, 120–133.
- de Loore C. 1970, "Convection regions and coronas of sun and stars," *Astrophys. & Space Sci.* **6**, 60–100.
- Dyt C. P. 1997, *Numerical simulations of supersonic turbulent convection and its relation to the modern Laplacian theory of solar system origin*, Ph.D thesis, Monash Univ., Victoria, Australia.
- Dyt C. P., Prentice A. J. R., 1998, "A numerical simulation of supersonic thermal convection," *Mon. Not. R. Astron. Soc.* **296**, 56–65.
- Fox P. A., Sofia S., Chan K. L., 1991, "Convective flows around sunspot-like objects," *Solar Physics* **135**, 15–42.
- Gough D. O., Moore D. R., Spiegel E. A., Weiss N. O., 1976, "Convective instability in a compressible atmosphere. II," *Astrophys. J.* **206**, 536–542.
- Hurlburt N. E., Toomre J., Massaguer J. M., 1984, "Two-dimensional compressible convection extending over multiple scale heights," *Astrophys. J.* **282**, 557–573.
- Jeans J. H., 1917, "The part played by rotation in cosmic evolution," *Mon. Not. R. Astron. Soc.* **77**, 186–199.
- Jeffreys H., 1918, "On the early history of the solar system," *Mon. Not. R. Astron. Soc.* **78**, 424–442.



- Kolmogorov A. N., 1941, "The local structure of turbulence in incompressible viscous fluid for very Large Reynolds numbers," *Dokl. Akad. Nauk SSSR* **30**, 301–305.
- Landahl M. T., Mollo-Christensen E., 1992, *Turbulence and Random Processes in Fluid Mechanics*, 2<sup>nd</sup> edn., Cambridge Univ. Press, Cambridge, U.K.
- Laplace P. S. de, 1796, *Exposition du Système du Monde*, Courcier, Paris, pp. 387–397.
- Lesieur M., 1997, *Turbulence in Fluids* 2<sup>nd</sup> edn. Kluwer Academic Publishers; The Netherlands.
- Lilly D. K., 1971, "Numerical simulations of developing and decaying two-dimensional turbulence," *J. Fluid Mech.* **45**, 395–415.
- Malagoli A., Cattaneo F., Brummell N. H., 1990, "Turbulent supersonic convection in three dimensions," *Astrophys. J.* **361**, L33–L36.
- Malhotra R., 1991, "Tidal origin of the Laplace resonance and the resurfacing of Ganymede," *Icarus* **94**, 399–412.
- Porter D. H., Woodward P. R., 2000, "Three-dimensional simulations of turbulent compressible convection," *Astrophys. J. Suppl. Series* **127**, 159–187.
- Prentice A. J. R., 1973, "On turbulent stress and the structure of young convective stars," *Astron. Astrophys.* **27**, 237–248.
- Prentice A. J. R., 1978a, "Origin of the solar system: gravitational contraction of the turbulent protosun and the shedding of a concentric system of gaseous Laplacian rings," *Moon and Planets* **19**, 341–398.

- Prentice A. J. R., 1978b, "Towards a modern Laplacian theory for the formation of the solar system," in S. F. Dermott (ed.), *The Origin of the Solar System*, John Wiley, New York, pp. 111–161.
- Prentice A. J. R., 1996a, "Origin and bulk chemical composition of the Galilean satellites and the primitive atmosphere of Jupiter: a pre-Galileo analysis," *Earth, Moon and Planets* **73**, 237–258.
- Prentice A. J. R., 1996b, "Internal structure and bulk chemical composition of Io: a pre-Galileo prediction," *Phys. Letts. A* **213**, 253–258.
- Prentice, A. J. R., 2001a, "Origin and bulk chemical composition of the Galilean satellites of Jupiter: a post-Galileo analysis," *Earth, Moon and Planets* **87**, 11–55.
- Prentice A. J. R., 2001b, "Gas ring condensation model for the origin and bulk chemical composition of Mercury," in *Workshop on Mercury: Space Environment, Surface, and Interior*, pp. 81–82. LPI Contribution No. 1097, Lunar and Planetary Institute, Houston.
- Prentice A. J. R., 2001c, "Origin and bulk chemical compositions of the inner planets," *Eos. Trans. AGU* **82** (47), Fall Meet. Suppl., Abstract P21B-0530.
- Prentice A. J. R., Dyt C. P., 2000, "Supersonic turbulent convection and the origin of the planets," *Bull. Amer. Astron. Soc.* **32**, 1102.
- Prentice A. J. R., ter Haar D., 1979, "Origin of the Jovian ring and the Galilean satellites," *Nature* **280**, 300–302.
- Smagorinsky I., 1963, "General circulation experiments with the primitive equations. I. The basic experiment," *Mon. Weath. Rev.* **91**, 99–164.

- Tittermore W. C., 1990, "Chaotic motion of Europa and Ganymede and the Ganymede-Callisto dichotomy," *Science* **250**, 263–267.
- Woolfson, M. M., 1978, "The capture theory and the origin of the solar system," in S. F. Dermott (ed.), *The Origin of the Solar System*, John Wiley, New York, pp. 179–198.
- Woolfson M. M., 1993, "The solar system—its origin and evolution," *Q. J. R. Astron. Soc.* **34**, 1–20.
- Woolfson M. M., 2000, "The origin and evolution of the solar system," *Astron. Geophys.* **41** (1), 12–19.
- Zalesak S. T., 1979, "Fully multidimensional flux-corrected transport algorithms for fluids," *J. Comput. Phys.* **31**, 335–362.



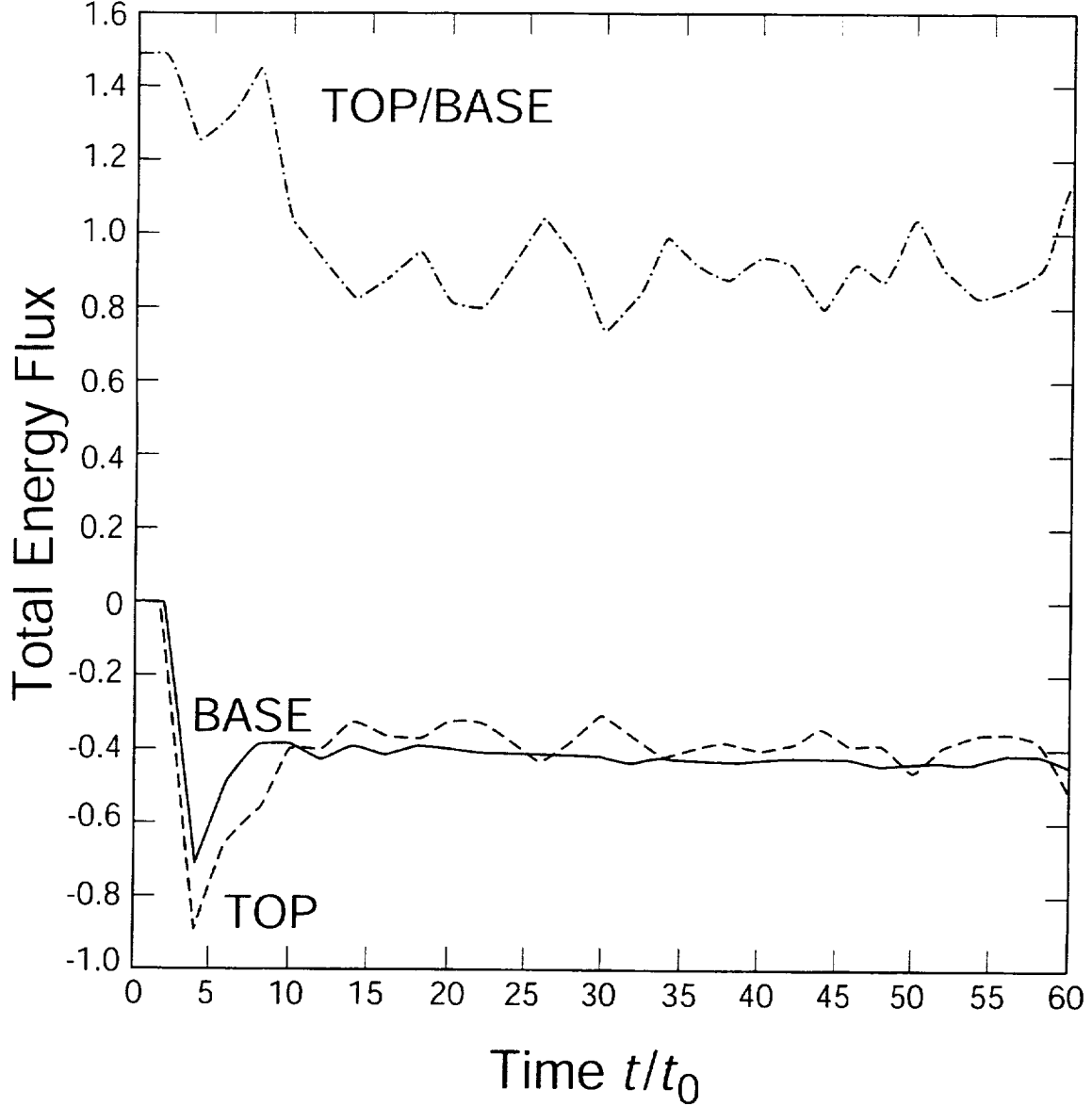


**Figure 1.** Plot of the total energy flux  $F_{\text{base}}$  entering the base of the atmosphere (curve marked BASE) and the total energy flux  $F_{\text{top}}$  leaving the top (curve marked TOP) plotted against elapsed time  $t$ . Also shown is a plot of the ratio  $F_{\text{top}}/F_{\text{base}}$ . At the top and bottom boundaries all energy is transmitted by the thermal diffusive flux  $F_{\text{diff}}$ , which is defined by equation (18). This flux varies with time, even after a quasi-equilibrium is established by time  $t = 10$ , since  $F_{\text{diff}}$  depends on the spatial gradient of the large-scale velocity field via the turbulent diffusivity  $\kappa_t$  (defined by equations (3)–(5)), and this field remains unsteady at all times. The physical unit of energy flux is  $\rho_0(\mathcal{R}T_0/\mu)^{3/2}$ , where  $\rho_0$  and  $T_0$  denote the initial density and temperature at the top boundary.

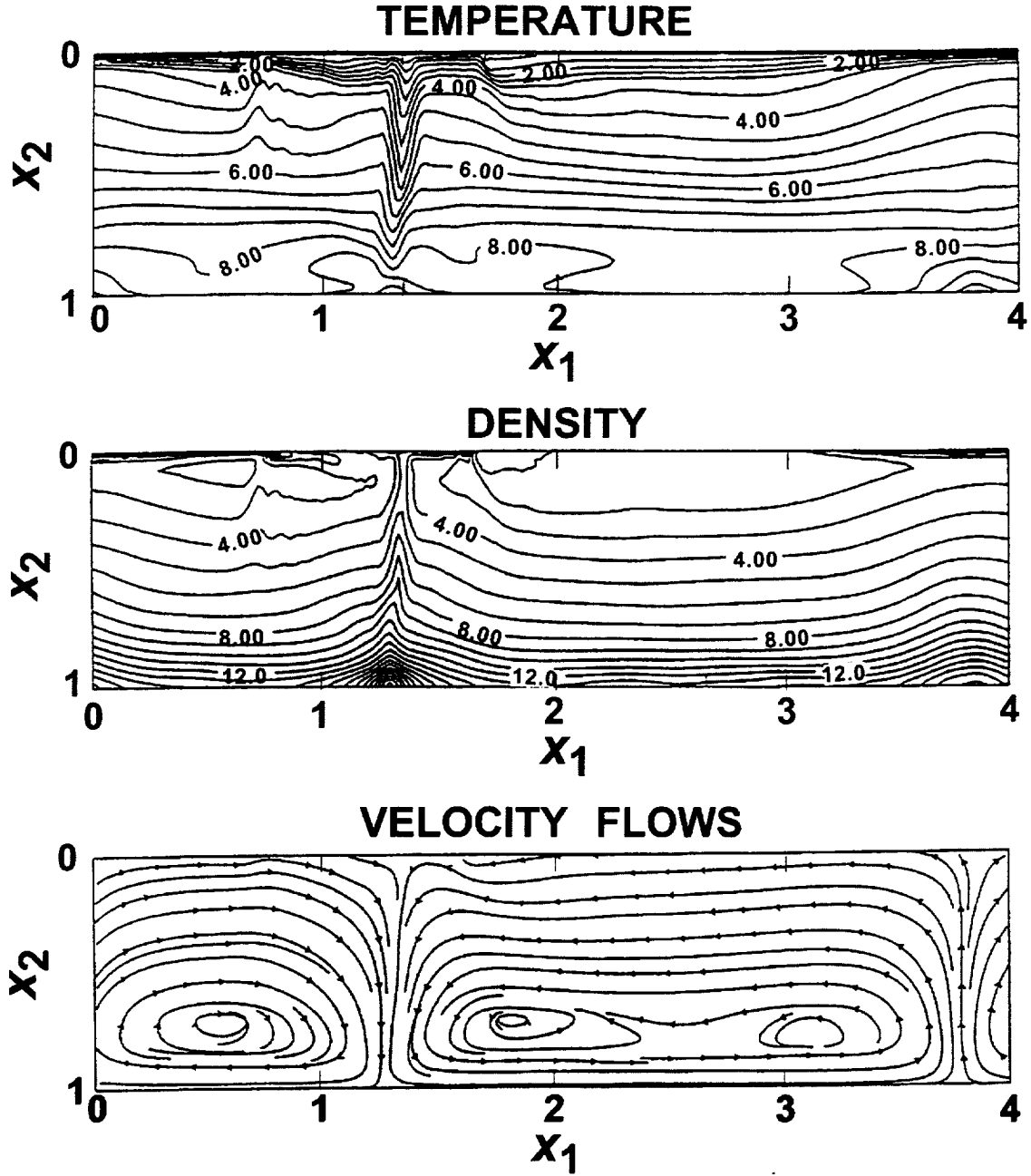


**Figure 2.** Contours of constant temperature and density in the model atmosphere at time  $t = 60$ . Here  $(x_1, x_2)$  are dimensionless Cartesian coordinates, and the convective flow is assumed to be horizontally periodic over a physical distance  $4d$  where  $d$  is the layer thickness. The bottom portion of the figure shows the streamlines of the velocity field. The diagram clearly illustrates the very strong downdraft of cold dense gas at  $x_1 \approx 1.3$  and the much weaker updraft of warm lighter gas at  $x_1 \approx 3.7$ .

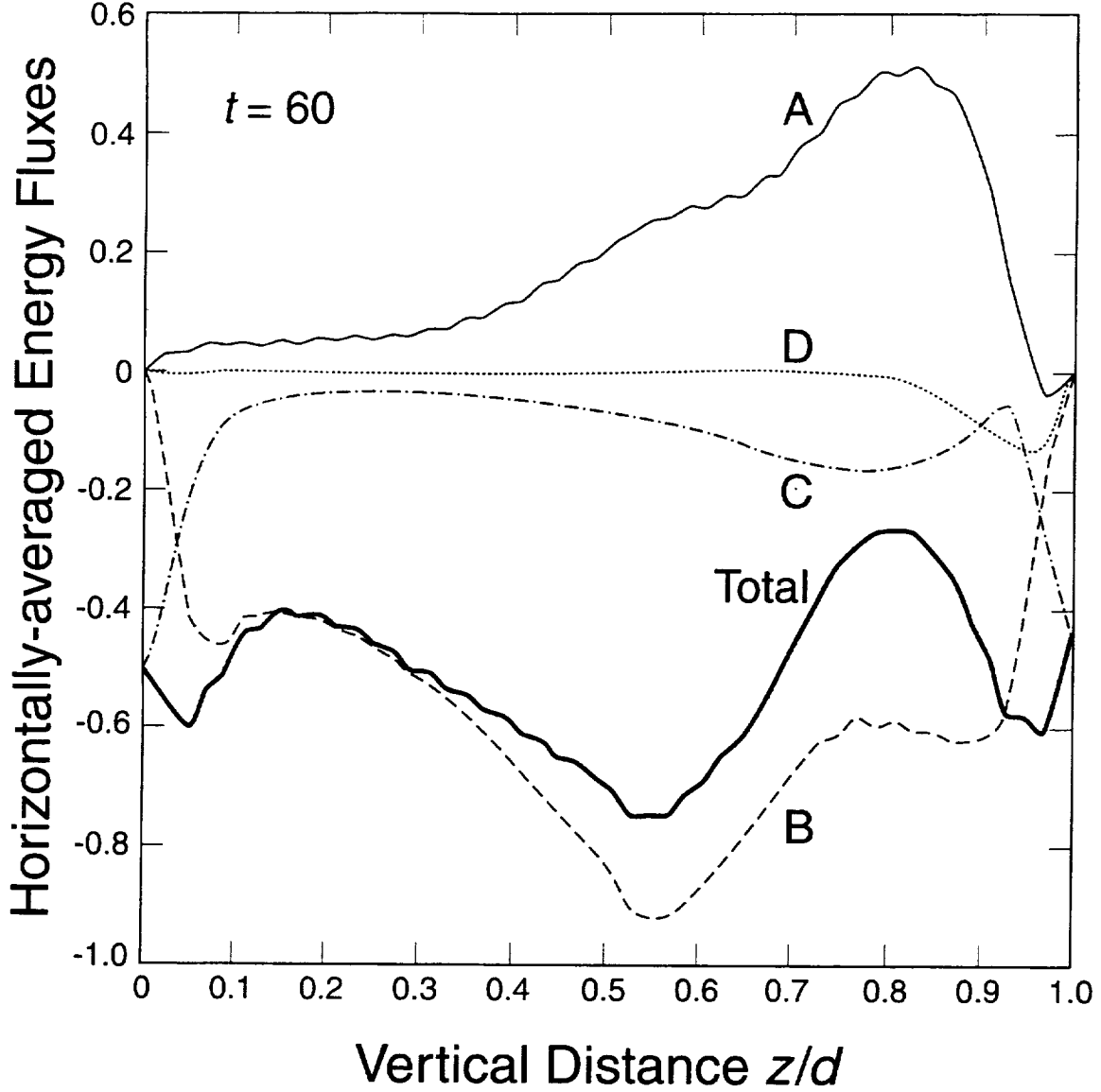


**Figure 3.** The four components and total of the vertical flux of energy through the atmosphere, plotted against vertical depth  $z$  at time  $t = 60$ . The curves marked A and B are the horizontal average of the kinetic energy flux  $F_{ke}$  and enthalpy flux  $F_{ep}$  as defined by equations (16) and (17). These depend directly on the velocity field  $u_i$  which is turbulent, so causing the small-scale fluctuations with depth. The other curves C and D show the horizontally-averaged thermal diffusion flux  $F_{diff}$  and viscous dissipation flux  $F_{visc}$  defined by equations (18) and (19). These fluxes exhibit less fluctuation with depth, and  $F_{visc}$  is negligible at most depths. At the top and bottom boundaries the convective fluxes vanish and all heat is transported by thermal diffusion. The heavy curve is the total energy flux  $F_{tot}$ , as given by equation (20).

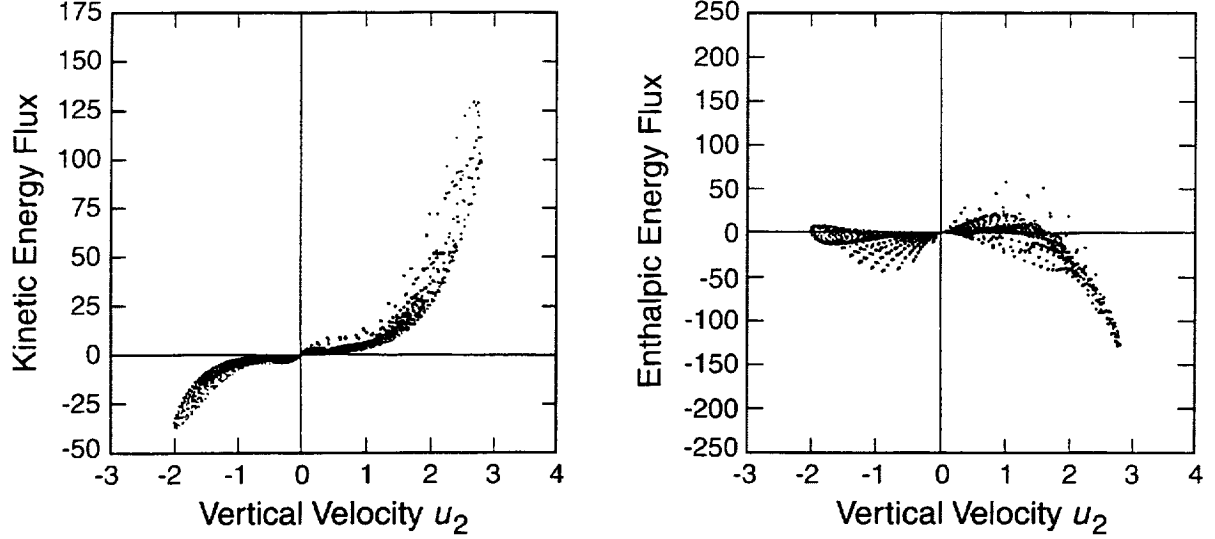


**Figure 4.** Phase diagrams of the kinetic energy flux components  $F_{ke}(i, j)$  and enthalpy flux components  $F_{ep}(i, j)$  plotted against dimensionless vertical velocity  $u_2$  at time  $t = 60$ . Each dot corresponds to a grid point  $(i, j)$  in the model atmosphere, with  $i = 1, 2, \dots, 200$  and  $j = 1, 2, \dots, 50$ . The physical unit of flux is  $\rho_0 (\mathcal{R}T_0/\mu)^{3/2}$  and that of velocity is  $(\mathcal{R}T_0/\mu)^{1/2}$ . It is clear from this diagram how the large flux of kinetic energy in the strong downflows is balanced out by a corresponding large upwards flux of enthalpy. The maximum downflow speed is  $u_2 = 2.8$ . It is associated with  $F_{ke} = 98.5$  and occurs at depth  $x_2 = 0.55$  where  $\rho = 9.0$ ,  $T = 4.8$  and the vertical Mach number is  $M = u_2/\sqrt{\gamma T} = 1.08$ . The maximum upflow speed is  $u_2 = -2.0$  where  $F_{ke} = -34.3$ . Here  $x_2 = 0.65$ ,  $\rho = 8.5$ ,  $T = 6.9$  and  $M = 0.65$ .



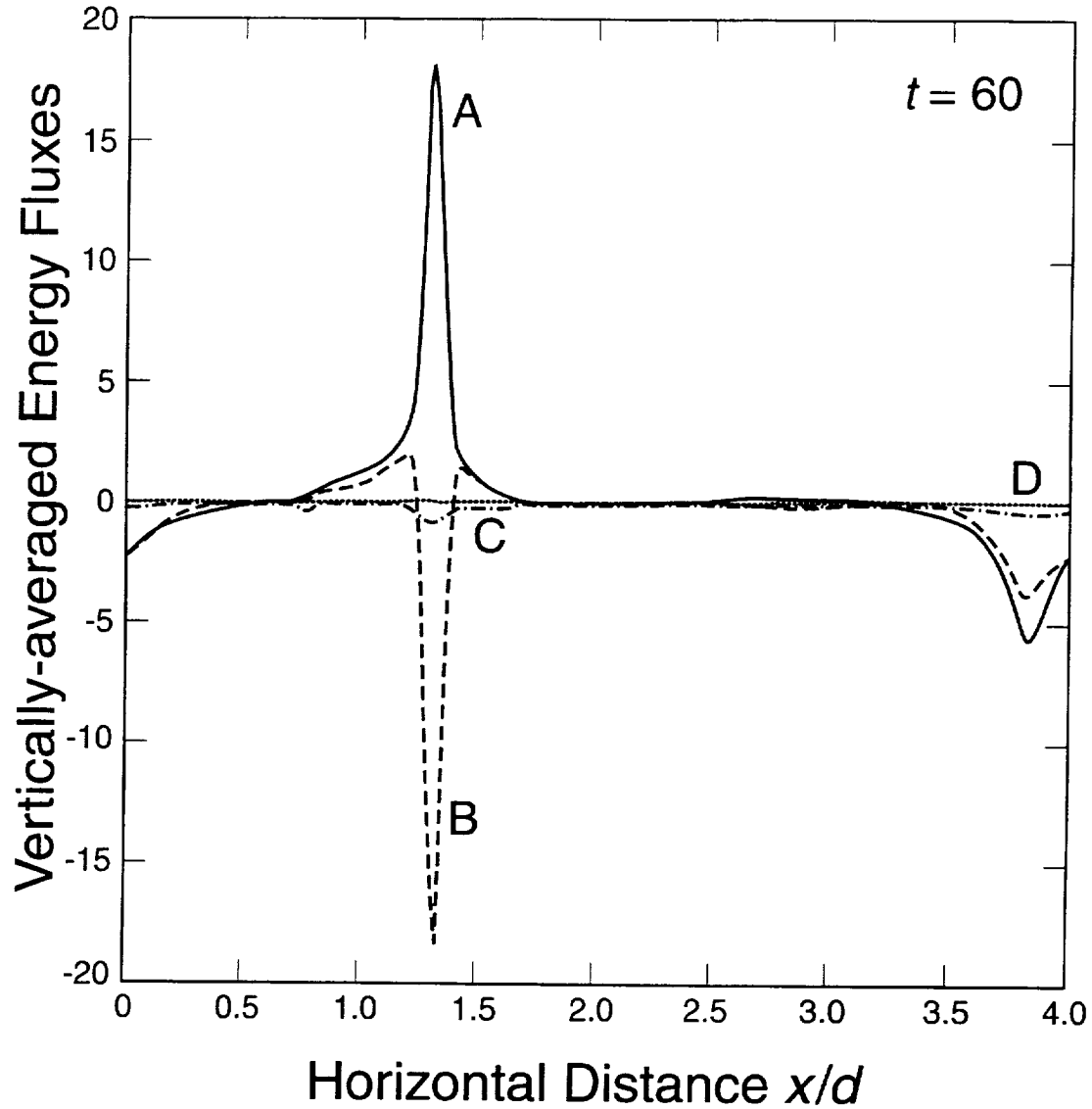


**Figure 5.** The four components of the vertical flux of energy plotted against the horizontal coordinate  $x$  in the model atmosphere. The curves marked A, B, C, D are the fluxes of kinetic energy, enthalpy, thermal diffusion, and viscous dissipation, respectively. They have been spatially averaged across the vertical coordinate  $z$  for each  $x$ . The most prominent feature to note in the diagram is the strong correlation between the kinetic energy and enthalpy fluxes.

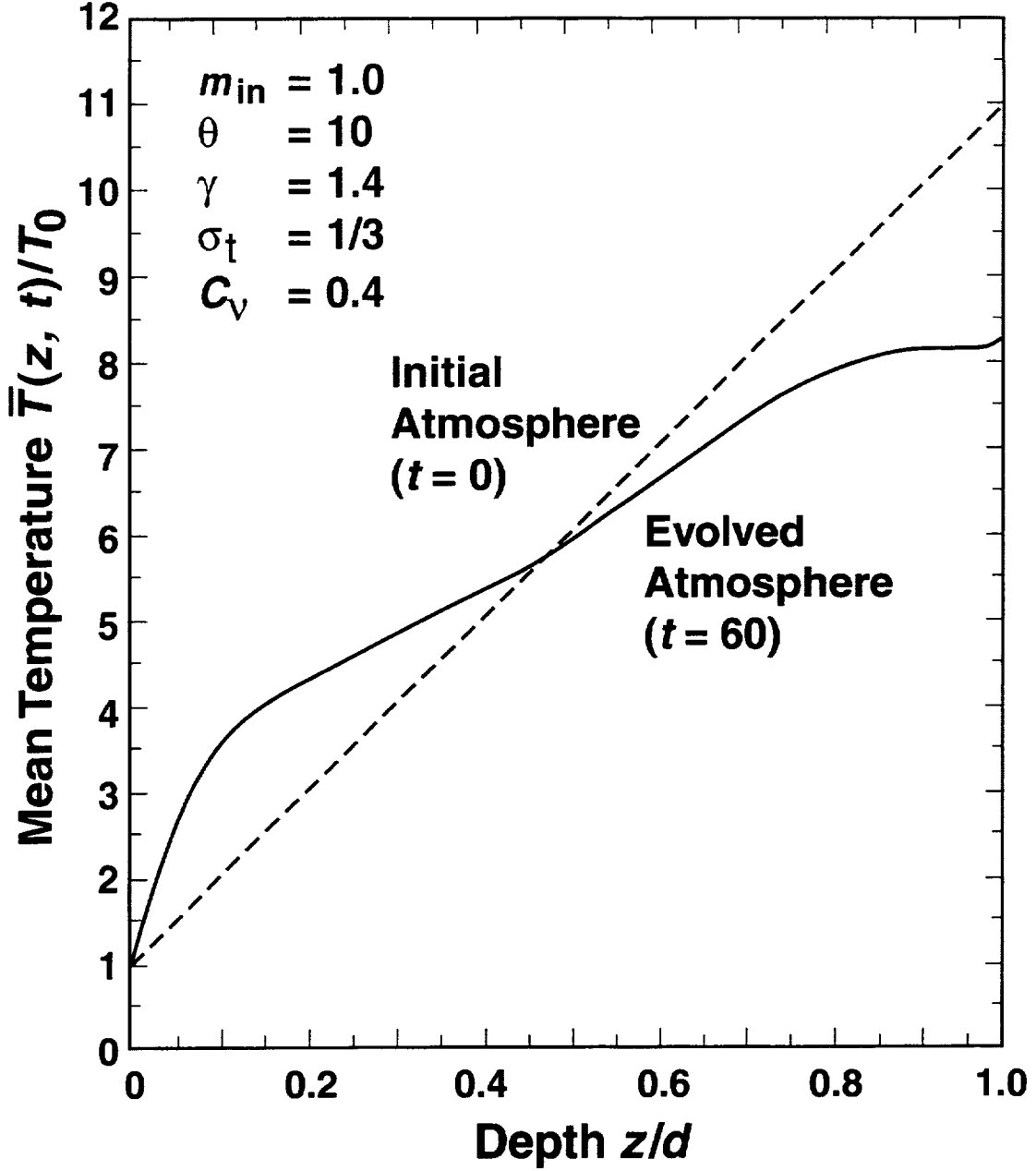


**Figure 6.** The horizontally-averaged temperature  $\bar{T}(z, t)$  versus depth  $z$  at times  $t = 0$  and  $t = 60$ . The onset of convection flattens the temperature gradient in the lower  $\sim 90$  percent of the atmosphere due to the destruction of the initial superadiabatic excess by the powerful downdraft of cold dense gas at  $x_1 = 1.3$ . At the very base of the atmosphere an increase of gradient is necessitated to meet the boundary condition  $\partial T / \partial z|_{z=d} = \theta T_0 / d$  specified by equation (15b). In the upper 10 percent of depth, however  $\partial \bar{T} / \partial z$  increases to  $\sim 3.3$  times the initial gradient  $\theta T_0 / d$  gradient, with  $\theta = 10$ , in order for the diffusive flux  $F_{\text{diff}} \propto \overline{\rho \kappa_1 \partial T / \partial z}$  to carry the total energy flux through the top boundary, where all of the convective fluxes are zero.

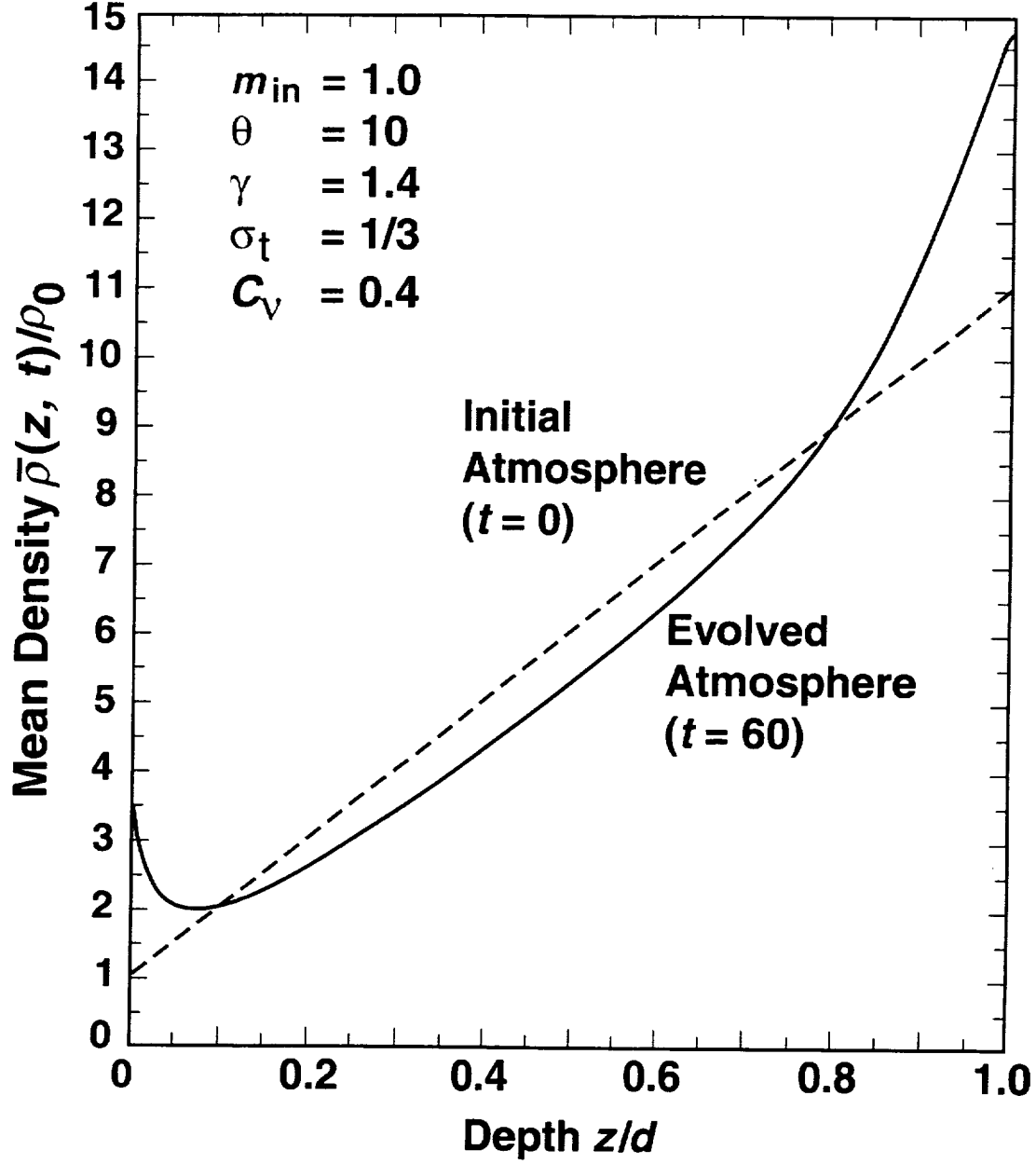


**Figure 7.** The horizontally-averaged mean density  $\bar{\rho}(z, t)$  versus depth  $z$  at times  $t = 0$  and  $t = 60$ . The prominent features to notice are (i) the steepening of the density gradient of the evolved atmosphere towards the base  $z = d$  due to the destruction of the initial superadiabatic excess of the lower atmosphere by the strong downdraft of negative enthalpy, and (ii) the existence of a density inversion at the top boundary. This latter phenomenon comes about because the mean temperature  $\bar{T}(z, 60)$  decreases so sharply as  $z \rightarrow 0$  that pressure balance necessitates a rise in density. Essentially, SGS modelling has greatly enhanced the mean level of superadiabaticity in the top layers to the point that the mean polytropic index  $\bar{m}(z, t) = \partial(\ln \bar{\rho}) / \partial(\ln \bar{T})$  becomes negative.

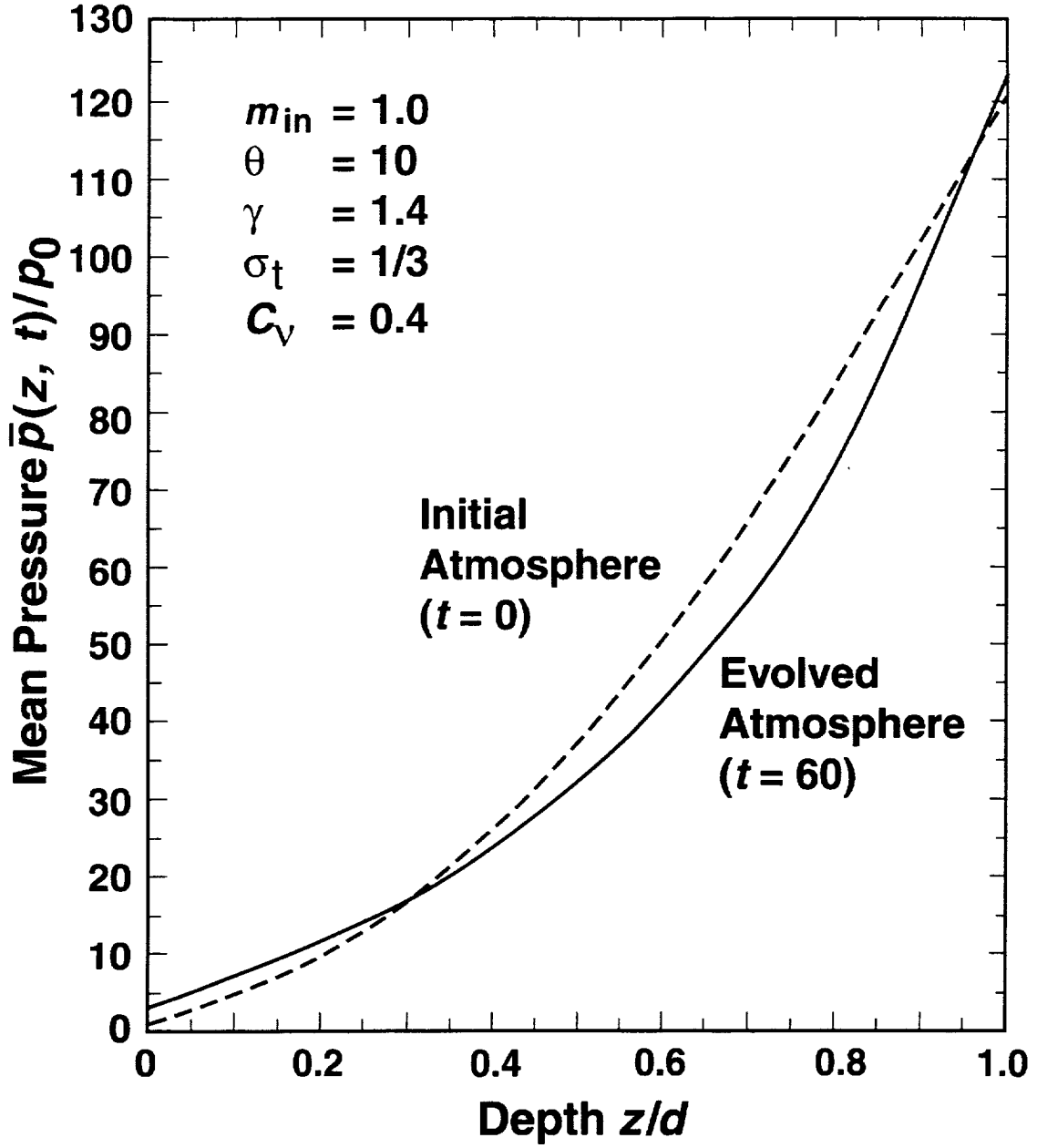


**Figure 8.** The run of the horizontally-averaged pressure  $\bar{p}(z, t)$  with depth  $z$  at times  $t = 0$  and  $t = 60$ . The unit of  $\bar{p}$  is the initial pressure  $p_0 = \rho_0 \mathcal{R}T_0/\mu$  at the top boundary. We see that  $\bar{p}(z, t)$  differs only modestly between the initial and evolved states compared to the radical changes exhibited by the mean density and temperature profiles (Figs. 6 and 7).

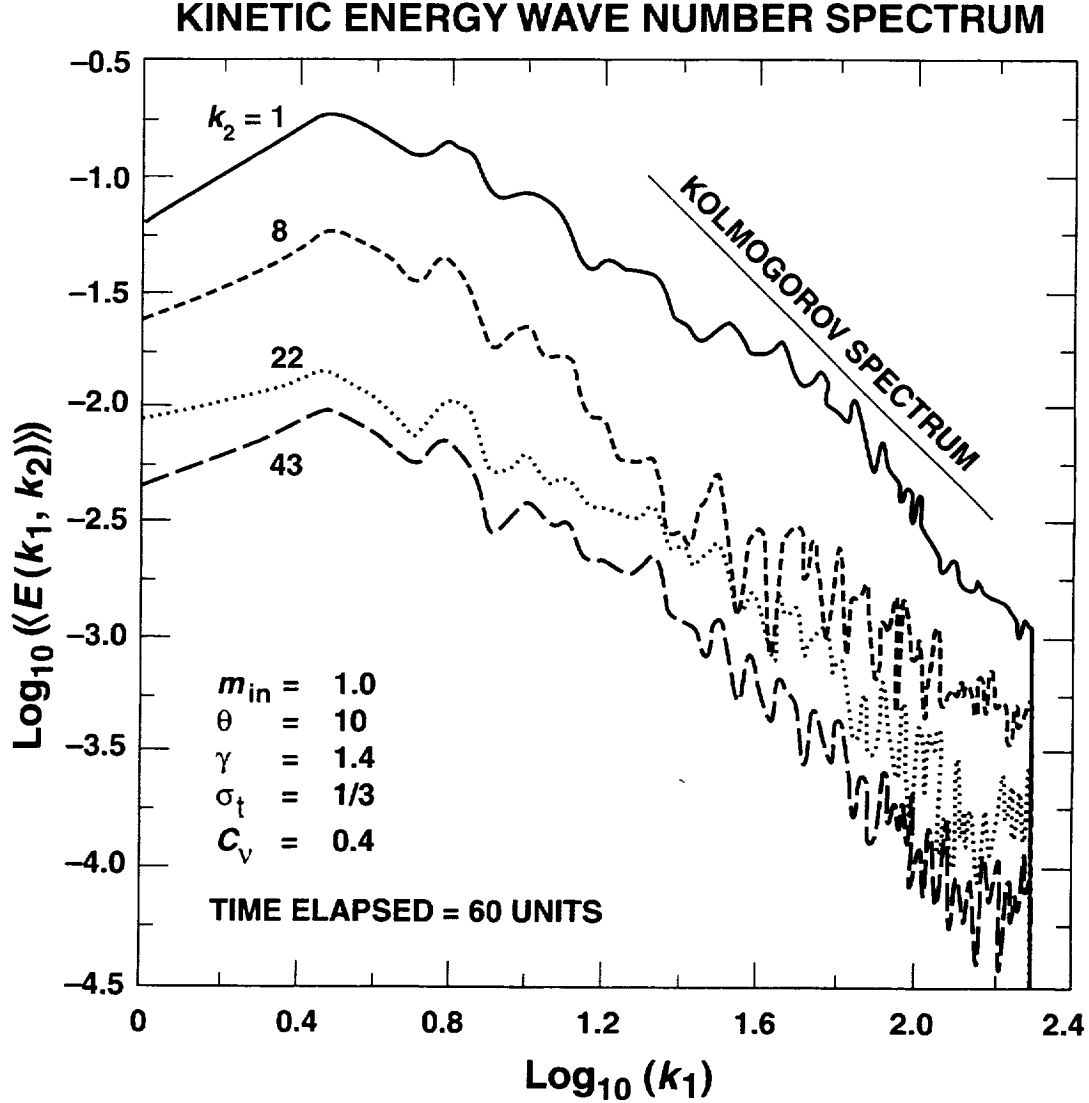


**Figure 9.** The globally-averaged wave number spectrum  $\langle E(k_1, k_2) \rangle$  of the specific kinetic energy  $\frac{1}{2}u^2$  plotted against the horizontal wave number  $k_1$  for various vertical wave numbers  $k_2$ . For the large values of  $k_2$  and  $k_1 \geq 20$ ,  $\langle E \rangle$  decays with  $k_1$  in accord with the Kolmogorov power law spectrum  $k_1^{-5/3}$  whose slope is indicated by the straight line segment in this bi-logarithmic plot. The fluctuations in  $\langle E \rangle$  are due to the turbulent character of the large-scale velocity field. The result confirms that the Smagorinsky formalism for modelling the influence of small-scale turbulent motions, whose wave numbers  $k_1$  exceed the grid cutoff wave number  $k_c = 200$ , is working correctly in this simulation. This situation comes about for the choice of the constants  $C_v = 0.4$  and  $\sigma_t = 1/3$ , as discussed in Section 3. That is, the rate of thermal energy production by viscous dissipation at large values of  $k_1$  matches the rate at which thermal energy is being injected back into the system as kinetic energy at smaller values of  $k_1$ , so producing the familiar Kolmogorov kinetic energy wave number spectrum.



REPORT DOCUMENTATION PAGE				Form Approved OMB No. 0704-0188	
Public reporting burden for this collection of information is estimated to average 1 hour per response, including the time for reviewing instructions, searching existing data sources, gathering and maintaining the data needed, and completing and reviewing the collection of information. Send comments regarding this burden estimate or any other aspect of this collection of information, including suggestions for reducing this burden, to Washington Headquarters Services, Directorate for Information Operations and Reports, 1215 Jefferson Davis Highway, Suite 1204, Arlington, VA 22202-4302, and to the Office of Management and Budget, Paperwork Reduction Project (0704-0188), Washington, DC 20503.					
1. AGENCY USE ONLY (Leave blank)		2. REPORT DATE 12/01/2001		3. REPORT TYPE AND DATES COVERED JPL Publication	
4. TITLE AND SUBTITLE A Numerical Simulation of Supersonic Turbulent Convection Relating to the Formation of the Solar System				5. FUNDING NUMBERS C - NAS7-1407 054500-3.3.33630	
6. AUTHOR(S) Andrew J. Prentice, C.P. Dyte					
7. PERFORMING ORGANIZATION NAME(S) AND ADDRESS(ES) Jet Propulsion Laboratory California Institute of Technology 4800 Oak Grove Drive Pasadena, CA 91109-8099				8. PERFORMING ORGANIZATION REPORT NUMBER JPL Publication 01-016	
9. SPONSORING / MONITORING AGENCY NAME(S) AND ADDRESS(ES) National Aeronautics and Space Administration Washington, DC 20546-0001				10. SPONSORING / MONITORING AGENCY REPORT NUMBER JPL Publication 01-016	
11. SUPPLEMENTARY NOTES					
12a. DISTRIBUTION / AVAILABILITY STATEMENT  SUBJECT CATEGORY: 91. lunar and planetary sciences DISTRIBUTION: Nonstandard AVAILABILITY: NASA CASI (301) 621-0390				12b. DISTRIBUTION CODE	
13. ABSTRACT (Maximum 200 words) A flux-corrected transport scheme is used to numerically simulate thermal convection in a two-dimensional layer of ideal, diatomic gas heated from below & stratified gravitationally across many pressure scale heights. This calculation mimics the conditions in the outer layers of the protosolar cloud [PSC] from which the Solar System formed. The temperature at the top boundary ( $z = 0$ ) & a dimensionless temperature gradient of 10 at the base of the layer of thickness $d$ are kept fixed with time. The initial atmosphere is uniformly superadiabatic, having polytropic index $m = 1$ . Because the Reynolds number of the real atmosphere is so large, a subgrid-scale [SGS] turbulence approximation is used to model of motions whose scale is less than the computational grid size. The flow soon evolves to a network of giant convective cells spanning the whole layer. At cell boundaries the downflows are narrow & rapid while the upflows are broad & sluggish. The peak downflow Mach number is $M = 1.1$ . The descent of the cold gas eliminates much of the initial superadiabatic structure of the lower atmosphere, so reducing the mean temperature gradient $DT$ & causing a rise in mean density $RHO$ towards the base. In the top 10% of depth, SGS modelling causes $DT$ to increase sharply. A steep density inversion occurs with $RHO$ rising to 3.5 times the initial value at the top boundary. This result gives credibility to the Modern Laplacian Theory [MLT] of Solar System origin. Here a postulated 35-fold density increase at the surface of the PSC causes the shedding of discrete gas rings at the observed mean orbital spacings of the planets. Even so, further simulations that may yield $M \sim 3$ & a top density upturn factor of 35 are needed for the MLT to be considered valid.					
14. SUBJECT TERMS lunar and planetary sciences, formation of the solar system, Laplace nebula model; 90. astrophysics, supersonic turbulent convection, flux-corrected transport algorithm				15. NUMBER OF PAGES 60	
				16. PRICE CODE	
17. SECURITY CLASSIFICATION OF REPORT Unclassified	18. SECURITY CLASSIFICATION OF THIS PAGE Unclassified	19. SECURITY CLASSIFICATION OF ABSTRACT Unclassified		20. LIMITATION OF ABSTRACT Unlimited	

